DESIGN OF A 3D INTEGRATED CIRCUIT FOR MANIPULATING AND SENSING BIOLOGICAL NANOPARTICLES

by

Samuel J. Dickerson

B.S. in Computer Engineering, University of Pittsburgh, 2003

Submitted to the Graduate Faculty of

the School of Engineering in partial fulfillment

of the requirements for the degree of

Master of Science

University of Pittsburgh

2007

UNIVERSITY OF PITTSBURGH

SCHOOL OF ENGINEERING

This thesis was presented

by

Samuel J. Dickerson

It was defended on

April 13, 2007

and approved by

Steven P. Levitan, Professor, Electrical and Computer Engineering (Thesis Co-Advisor)

Donald M. Chiarulli, Professor, Computer Science (Thesis Co-Advisor)

William Stanchina, Chairman and Professor, Electrical and Computer Engineering

Kevin P. Chen, Assistant Professor, Electrical and Computer Engineering

DESIGN OF A 3D INTEGRATED CIRCUIT FOR MANIPULATING AND SENSING BIOLOGICAL NANOPARTICLES

Samuel J. Dickerson, M.S.

University of Pittsburgh, 2007

We present the design of a mixed-technology microsystem for electronically manipulating and optically detecting nanometer scale particles in a fluid. This lab-on-a-chip is designed using 3D integrated circuit technology. By taking advantage of processing features inherent to 3D chip-stacking technology, we create very dense dielectrophoresis electrode arrays. During the 3D fabrication process, the top-most chip tier is assembled upside down and the substrate material is removed. This puts the polysilicon layer, which is used to create geometries with the process' minimum feature size, in close proximity to a fluid channel etched into the top of the stack. This technique allows us to create electrode arrays that have a gap spacing of 270 nm in a 0.18 μm SOI technology. Using 3D CMOS technology also provides the additional benefit of being able to densely integrate analog and digital control circuitry for the electrodes by using the additional levels of the chip stack.

For sensing particles that are manipulated by dielectrophoresis, we present a method by which randomly distributed nanometer scale particles can be arranged into periodic striped patterns, creating an effective diffraction grating. The efficiency of this grating can be used to perform a label-free optical analysis of the particles.

The functionality of the 3D lab-on-a-chip is verified with simulations of Kaposi's sarcoma-associated herpes virus particles, which have a radius of approximately 125 nm, being manipulated by dielectrophoresis and detected optically.

TABLE OF CONTENTS

LIST OF TABLES

LIST OF FIGURES

PREFACE

I would first like to thank my advisors, Dr. Steven Levitan and Dr. Donald Chiarulli. Most graduate students get one advisor throughout their academic career, but I've been fortunate to have two great ones. Special thanks to Steve for taking me into his research group and to Don for making sure I never have a dull moment.

I would also like to thank Sandy, Joni, Theresa, Bill and Jim for all the assistance they've given me in my day-to-day activities, without whom the third floor of Benedum hall would be in chaos.

I especially would like to thank all of the many other students with whom I've had the pleasure to work with throughout the years, Bryan, Jose, Mike, Majd, Arnaldo, Joel and Ben. Each of them are unique folks whom, as much as I try to, I will never forget. A special thanks to Jason for selflessly giving of himself to me and others with whatever oddball task we bother him with.

I would like to thank Aunt Carolyn and Papa for their support. Thanks to Aunt Joan for her parking space and suggestion to "go to college". I would like to thank Isaac for giving me an early start on my way to geekiness with his comic book movies and video games, making me fit in with the other engineers. Thanks to mom and dad for being the best parents ever, and keeping me supplied with vitamins to keep my brain going.

Finally, I would like to thank the most important person to me, a person so important that not only do they get their own paragraph in my thesis; but their own page, my wonderful wife Naomi. Without her I would probably starve, stink, and wear wrinkled clothes (more often) and just wouldn't enjoy things as much, you truly are the best wife.

-Sam

1.0 INTRODUCTION

In this thesis, we present the design of a lab-on-a-chip that can manipulate biological particles that are on the same size scale as viruses and propose a new method for sensing them. Lab-on-a-chip devices are an emerging microsystem technology for which the goal is to integrate multiple laboratory functions on to a single chip (figure 1.1). These chips are primarily used to assay biological particles. They can perform functions such as sample preparation, microfluidic transport, synthesis, analysis and detection.

Figure 1.1 Illustration of the goal of lab-on-a-chip microsystems, to integrate multiple laboratory functions onto a single chip [44],[45].

There are many advantages that come from the miniaturization of biological laboratory functions [46]. For example, it reduces sample size requirements, as only nano-liter or pico-liter

volumes are needed to carry out an analysis. Lab-on-a-chip microsystems are capable of performing high-throughput analyses, reducing the required processing time from hours to a matter of seconds. These devices allow for experimentation to be done with superior resolution, allowing for isolation and manipulation of single biological particles such as cells and viruses. Furthermore, lab-on-a-chip microsystems are cost-efficient because electronics can be integrated onto them and they are fabricated using processes in which they can be mass-produced. All of these factors make the future of lab-on-a-chip microsystems bright. One recent market analysis reports that applications of microfluidics to the life sciences have a global market that could rise to around 1.9 billion U.S. dollars by 2010[47]. In addition, the availability of devices that can automatically perform rapid diagnostics in a compact, inexpensive package is going to be particularly beneficial to countries in the developing world that lack the infrastructure to support modern medical technologies [44].

Dielectrophoresis is used in a broad range of lab-on-a-chip applications such as cytometry, cell sorting, and mixture separation. It is the physical phenomena where electric fields are used to control the movement of particles that are in a fluid. The technique has been shown to be a viable method for manipulating small particles without the need for contact [1,2,3] and it is the method used by the lab-on-a-chip presented in this thesis. Current dielectrophoresis-based lab-on-a-chip implementations have primarily focused on the manipulation of cells and have already been found to be promising for furthering cancer research [4,5,6,7]. Part of our research goals is to apply these techniques to smaller particles, such as viruses and macromolecules.

Kaposi's sarcoma-associated herpes virus (KSHV) is a recently discovered DNA virus that causes disease in humans [8]. KSHV is one of the most interesting subjects in molecular virology because it is one of the few examples of a virus that can cause cancerous tumors. The

study of KSHV allows researchers to form a link between the structure of tumor viruses and modern cancer biology [9]. KSHV is a spherical virion that has a radius of approximately 125 nm (figure 1.2). KSHV's extremely small size creates the need for instrumentation that will allow it to be efficiently manipulated and analyzed. We use KSHV as a model for the kinds of biological particles we would like to manipulate and detect with our lab-on-a-chip design.

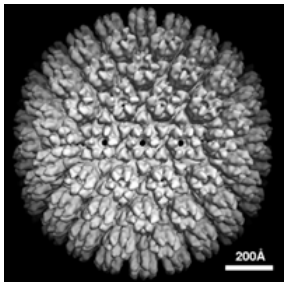

Figure 1.2. Image of one KSHV virion [10]

One trend of microelectronics research is similar to that of biomedical research in that both technologies are scaling downwards in size (figure 1.3). However, current technology limitations restrict most lab-on-a-chip devices to fabricating dielectrophoresis electrodes that are not well-suited for the manipulation of biological nanoparticles, such as viruses. Figure 1.3 shows a depiction of a typical integrated circuit. Integrated circuits are fabricated by using photolithography to pattern multiple layers that are used to create active devices and interconnect. The topmost layer patterned on an integrated circuit, used for external I/O, can only be fabricated at micron-scale dimensions and is the design layer that is most commonly used to create lab-on-a-chip electrodes. Even for advanced technologies, the design layers that are used to create geometries with nano-scale feature sizes are located towards the bottom of a chip and are surrounded by a thick substrate layer, making them inaccessible for use as electrodes. These restrictions make it a challenge to implement a system that can efficiently manipulate nanometer scale biological particles using conventional integrated circuit technology.

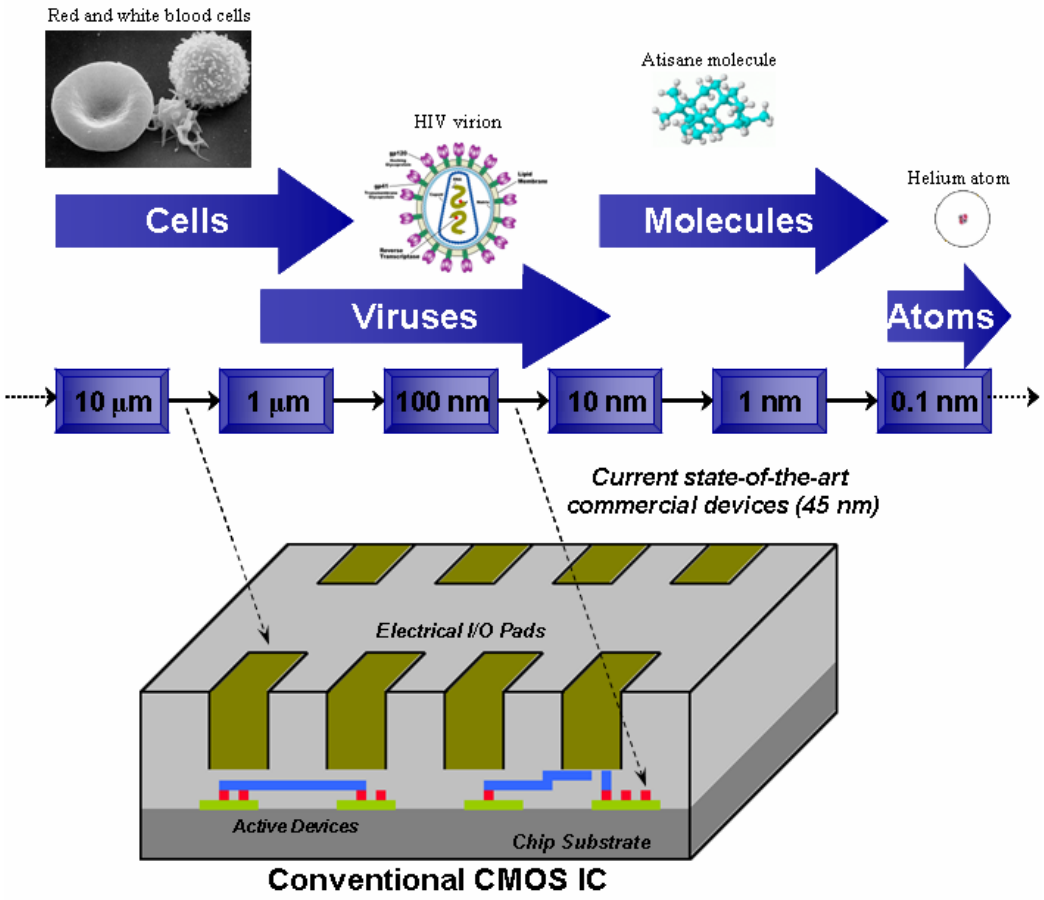

Figure 1.3. Illustration of biological scaling versus integrated circuit technology scaling [38]

Another challenge facing the development of lab-on-a-chip devices is the development of detection mechanisms that are inexpensive and non-invasive. Microscopy techniques are non-invasive but, they are costly and not suitable for use in a mobile device. The technique of labeling particles (fluorescence, magnetic, etc.) is a low-cost detection solution but, it often requires that the analyte be modified in some unnatural way and is also not well-suited for use outside of a laboratory setting.

Overcoming these two challenges gives the motivation for this work: The design of a dielectrophoresis-based lab-on-a-chip that can efficiently manipulate and detect nanometer scale particles (figure 1.4). The lab-on-a-chip is designed using 3D integrated circuit technology, in

which chips are stacked vertically. We take advantage of fabrication features found in this technology to create a high-density electrode array for dielectrophoresis. In addition to manipulating nanometer scale biological particles, we also present a new label-free optical detection scheme for sensing particles on lab-on-a-chip microsystems.

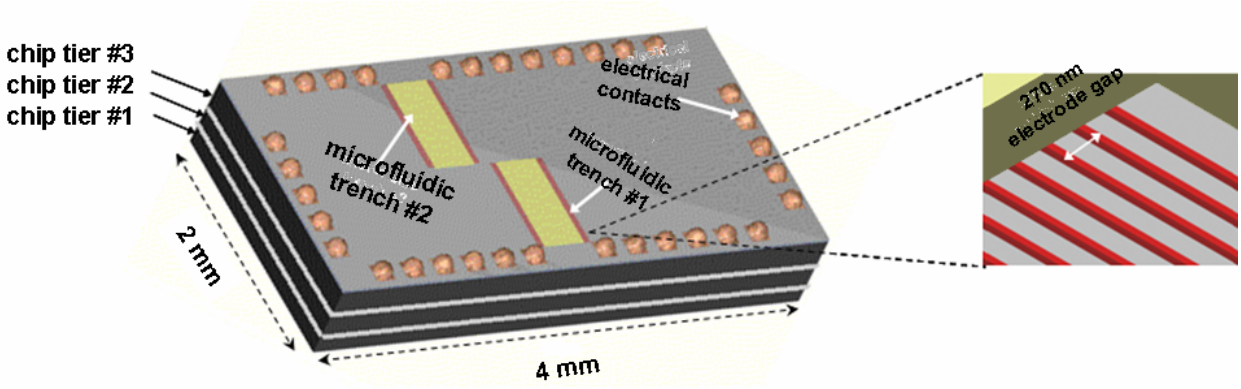

Figure 1.4. 3D lab-on-a-chip presented in this work. Inset shows a close-up view of its high-density electrode array.

1.1 PROBLEM STATEMENT

The research questions we address in this thesis are: What is the best way to design a lab-on-a-chip that can efficiently manipulate virus-sized particles? How can information about nanometer scale particles being manipulated by the lab-on-a-chip be analyzed in a practical way? And finally, how can the behavior of a lab-on-a-chip microsystem that operates in many physical domains be accurately modeled?

1.2 STATEMENT OF WORK

In order to answer the aforementioned questions, we performed the following tasks:

- **Design of 3D lab-on-a-chip**: We designed a dielectrophoresis-based lab-on-a-chip using 3D integrated circuit technology. The design includes an electrode array for dielectrophoresis, microfluidic trenches, digital circuits and analog electronics. The GDSII layout of the design was submitted to be fabricated in MIT Lincoln Labs 0.18 μm SOI 3D process.

- **Development of technique for detection of nanometer scale particles:** We developed a novel scheme for detecting biological particles on lab-on-a-chip microsystems. We show how very small particles can be manipulated such that they can be detected using conventional diffractive optics.

- **Modeling of 3D lab-on-a-chip:** We verified the functionality of the lab-on-a-chip by performing a simulation study of it manipulating Kaposi's sarcoma-associated herpes virus particles. This task includes the use of multiple CAD tools to characterize the behavior of our system in the electronic, electrostatic, optical, thermodynamic, microfluidic and mechanical domains. We also wrote a custom discrete-time simulator that uses these simulation results to model the movement of the particles within the microfluidic trench.

1.3 KEY CONTRIBUTIONS

From the results of our work, we make the following research contributions:

- **Novel lab-on-a-chip design**: This is the first lab-on-a-chip to be implemented using 3D integrated circuit technology. In the design, we introduce innovative concepts for creating on-chip electrode arrays and microfluidic channels. Our design also demonstrates the advantages that 3D integration provides in terms of adding robust functionality to lab-on-a-chip devices.

- **New technique for detection of nanometer scale particles:** We provide a new, cost-effective solution to sensing extremely small particles on lab-on-a-chip microsystems. Our technique avoids the use of expensive equipment to collect information about particles that are below the diffraction limit of optical microscopes. The technique we devised is especially well suited for biological particles.

- **Methodology for simulating lab-on-a-chip microsystems:** We show how a lab-on-a-chip microsystem that simultaneously interacts in many domains can be accurately modeled by using various CAD tools for each of those domains and then integrating the results with the use of a custom tool.

1.4 THESIS ROAD MAP

The rest of this thesis organized as follows: Chapter 2 gives a theoretical background of dielectrophoresis and discusses some of the issues that arise when dielectrophoresis is used to control nanometer scale particles. Detailed descriptions of the lab-on-a-chip architecture and fabrication procedures are provided in chapter 3. Chapter 4 shows the technique we developed to sense particle samples on lab-on-a-chip microsystems with diffractive optics. Chapter 5 presents the results from a simulation study of the lab-on-a-chip manipulating and detecting KSHV particles. Post-fabrication procedures and a test plan for the initial prototypes are given in chapter 6. Finally, we present a summary of our work and conclusions in Chapter 7, followed by a discussion of possible future directions.

2.0 THEORY OF DIELECTROPHORESIS

In this chapter, we provide an overview of the theory behind the central mechanism we use to manipulate particles, dielectrophoresis (DEP). Dielectrophoresis is the physical phenomenon whereby a particle with no net charge undergoes motion in response to a spatially non-uniform electric field [11]. When an electrically neutral particle is placed in the presence of a set of electrodes configured to create a non-uniform electric field, the particle becomes polarized. As a result of this polarization (figure 2.1), the negative charges are separated by a small distance from the positive charges and because the particle is neutral, the two charges on the body are opposite but equal in magnitude.

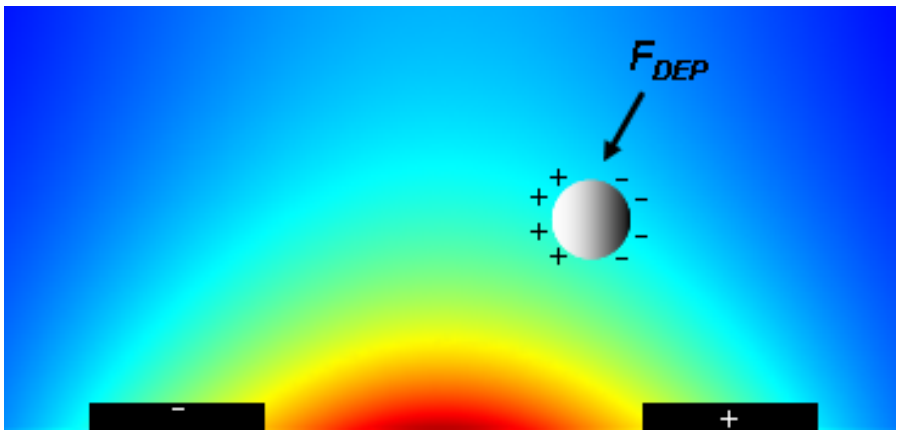

Figure 2.1 Electrically neutral particle in the presence of a spatially non-uniform electric-field. The dipole moment induced within the particle results in a translational force.

In order to derive the translational force that causes the particle to move, the polarized body can be modeled as a small physical dipole [12]. The force on an infinitesimal dipole is

$$\vec{F}_{dipole} = \vec{p}_{eff} \cdot \nabla \vec{E} \tag{2.1}$$

Equation (2.1) shows that there is no net force on a dipole unless the externally imposed electric field is nonuniform. In the case of a sphere suspended in a dielectric medium (for dielectrophoresis, the medium is typically an aqueous solution), the effective dipole moment induced by the electric field $\vec{E}$ is defined as

$$\vec{p}_{eff} = 4\pi r_p^{\,3} \varepsilon_m \left(\frac{\varepsilon_p^* - \varepsilon_m^*}{\varepsilon_p^* + 2\varepsilon_m^*} \right) \vec{E} \tag{2.2}$$

where r_p is the radius of the particle, ε_m is the permittivity of the medium and $\varepsilon_p^*, \varepsilon_m^*$ represents the complex permittivities of the particle and medium respectivly. Complex permittivity is a function of an objects conductivity σ and is given by

$$\varepsilon^* = \varepsilon - j\frac{\sigma}{\omega} \tag{2.3}$$

at an angular frequency of ω. From equations (2.1) and (2.2) the expression for the time averaged force exerted on the particle in an AC field is:

$$\left\langle \vec{F}_{DEP} \right\rangle = 2\pi \varepsilon_m r_p^{\,3} \, \mathrm{Re}\left[K_{CM}\right] \nabla E_{RMS}^2 \tag{2.4}$$

where

$$K_{CM} = \frac{\varepsilon_p^{\,*} - \varepsilon_m^{\,*}}{\varepsilon_p^{\,*} + 2\varepsilon_m^{\,*}} \tag{2.5}$$

The term K_{CM} is known as the Clausius-Mossotti factor [12] and is a measure of relative permittivities between the particle and the surrounding medium. It can be seen from equations (2.4) and (2.5) that this factor determines the direction of the dielectrophoretic force. When the

sign of $Re[K_{cm}]$ is positive, the particle is more polarizable than its surrounding medium and it undergoes what is known as positive dielectrophoresis (pDEP). While undergoing positive dielectrophoresis, the force vector is directed along the gradient of electric field intensity ∇E_{RMS}^2. Under these conditions, the particles are attracted to the locations of electric field intensity maxima and repelled from the minima. The opposite occurs when $Re[K_{cm}]$ is negative, referred to as negative dielectrophoresis (nDEP).

Dielectrophoresis techniques work for both AC and DC excitations of the electric field. By substituting equation (2.3) into (2.5), the high and low frequency limits for $Re[K_{cm}]$ are found to be

$$\lim_{\omega \to 0} \mathrm{Re}\left[K_{CM}\right] = \frac{\sigma_p - \sigma_m}{\sigma_p + 2\sigma_m} \tag{2.6}$$

$$\lim_{\omega \to \infty} \mathrm{Re}\left[K_{CM}\right] = \frac{\varepsilon_p - \varepsilon_m}{\varepsilon_p + 2\varepsilon_m} \tag{2.7}$$

Equations (2.6) and (2.7) show that the relative difference in ohmic losses dominates the low frequency behavior of $\vec{F}_{DEP}$, while dielectric polarization effects are more significant at high frequencies. These equations also show that $Re[K_{cm}]$ is bounded ($-\frac{1}{2} < Re[K_{cm}] < 1$) regardless of frequency. Figure 2.2 shows an example dielectrophoretic spectrum with $\sigma_p < \sigma_m$ and $\varepsilon_p > \varepsilon_m$. For this case, the particles would move under the influence of nDEP forces at low frequencies and pDEP forces at all frequencies above the zero-crossing of $Re[K_{cm}]$.

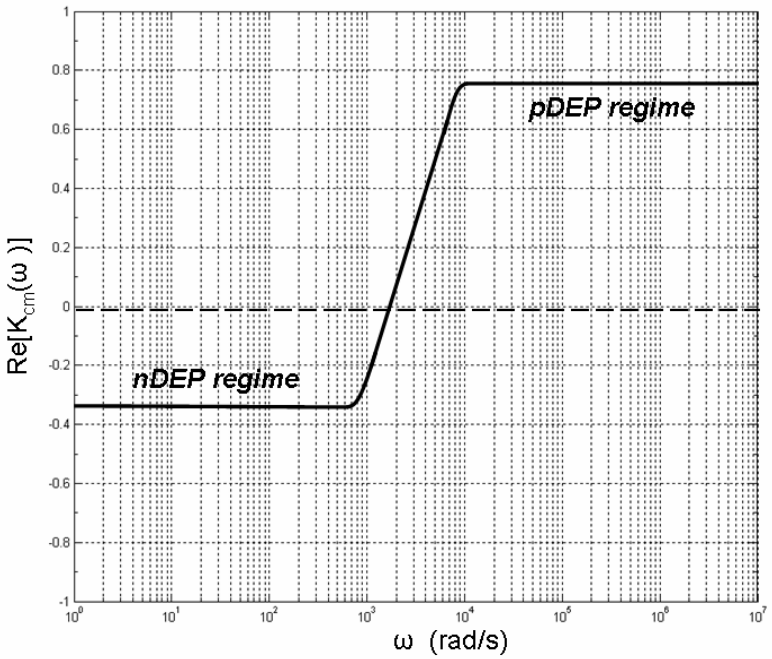

Figure 2.2 Example dielectrophoretic spectrum with $\sigma_p < \sigma_m$ and $\varepsilon_p > \varepsilon_m$

In summary, from equations (2.4)-(2.7) we observe the following main features of dielectrophoresis:

- $\vec{F}_{DEP}$ is present only when the electric field is spatially nonuniform.
- $\vec{F}_{DEP}$ can be observed with AC as well as DC excitations of the electric field.
- $\vec{F}_{DEP}$ is not affected by the polarity of $\vec{E}$. It depends only on $\left|\vec{E}\right|$ or $\vec{E}_{RMS}$
- $\vec{F}_{DEP}$ is directly proportional to the volume of the particle.
- $\vec{F}_{DEP}$ direction depends on the relative permittivities, as indicated by K_{cm}
    - pDEP forces ($Re[K_{cm}] > 0$) cause particles to move towards the regions with the strongest electric field strength.
    - nDEP forces ($Re[K_{cm}] < 0$) cause particles to move towards the regions with the weakest electric field strength.

2.1 FORCES EXERTED ON NANOSCALE PARTICLES

Particles actuated by dielectrophoresis move in a fluidic medium, therefore other forces have to be taken into consideration when describing their motion (figure 2.3). The most considerable of which are the hydrodynamic forces. The velocity of the particles will be significantly slowed by the resistance of drag forces while buoyancy forces may cause them to naturally float. In addition to these, under certain conditions forces that have been considered insignificant when manipulating micron scale particles (e.g. cells) can become more pronounced at the nanometer scale (e.g. viruses). This includes both electro-thermal effects that induce additional drag and random Brownian forces. These effects have been observed experimentally [13,14,15]. If the dielectrophoretic force is not strong enough, these forces will cause the particles to move at unreasonably slow speeds, move to unintended locations or, possibly, not move at all.

In this section, we provide a brief review of these forces as they relate to dielectrophoresis. Full derivations are not provided and other references are suggested. See references [14,16,17] for a more complete treatment.

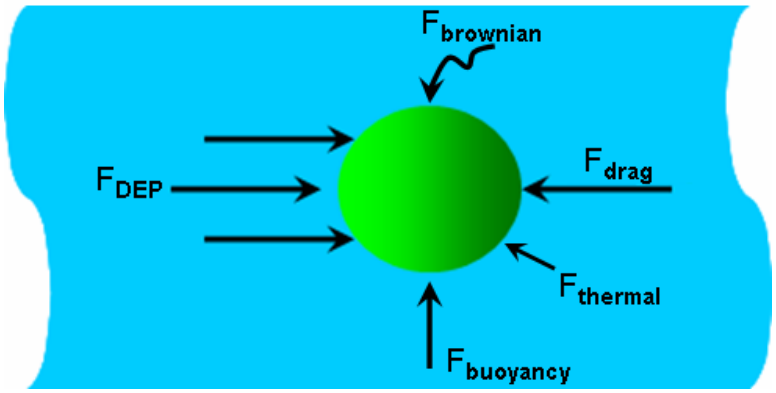

Figure 2.3 Forces exerted on a particle moving in fluid, under the influence of dielectrophoresis

2.1.1 Hydrodynamic forces

In fluid mechanics, the Reynolds number is the ratio used to measure the relative importance of inertial forces to viscous forces and is defined as [18]

$$Re = \frac{\rho_m L v_m}{\eta_m} \tag{2.8}$$

where ρ_m is the fluid density, v_m is the mean fluid velocity, L is the characteristic length of the system and η_m is the dynamic fluid viscosity. Nanometer scale particles have very small Reynolds numbers; therefore they experience laminar Stokes flows in which inertia is negligible [18].

The motion of fluids is described by a set of partial differential equations known as the Navier-Stokes equations. For the case of a small Reynolds number sphere undergoing laminar flow in an incompressible, Newtonian fluid, these equations reduce to a simple closed form [18]. Since we are manipulating nanometer scale biological particles in an aqueous medium that meets the previously mentioned criteria (e.g. water or a KCL buffer solution) we can model the drag force exerted on the moving particles using Stoke's law:

$$F_{drag} = 6\pi\eta_m r_p \left(v_m - v_p\right) \tag{2.9}$$

where v_p is the velocity of the particle. Stokes's law has been experimentally verified to be an accurate estimate of the drag force when $Re < 0.5$ and deviates by only about 10% at $Re = 1$ [19].

The other hydrodynamic force exerted on particles manipulated by dielectrophoresis is buoyancy [16]

$$F_{buoy} = V_p\left(\rho_p - \rho_m\right)g \tag{2.10}$$

where g is the acceleration due to gravity and the ρ_p and V_p represent the density and volume of the particle. Since the volume of a nano-particle is small, the magnitude of the buoyancy force is

also small. However, the densities may be such that $\vec{F}_{DEP}$ will have to overcome particles natural tendency to float or sediment over time.

2.1.2 Electro-thermal forces

The high intensity electric fields often needed to manipulate particles have been observed to produce joule heating inside the fluidic medium [13,15], especially when dielectrophoresis is occurring at AC frequencies in the MHz range. This ohmic heating causes a temperature gradient that in turn results in spatial conductivity and permittivity gradients within the suspending medium. The variation of electrical properties within the medium results in coulombic and dielectric body forces that will induce extra fluid flow. The time-averaged body force on the fluid is given by [20]

$$\left\langle \vec{F}_{thermal} \right\rangle = \frac{1}{2} Re\left[\frac{\sigma_m \varepsilon_m (\alpha - \beta)}{\sigma_m + i\omega\varepsilon_m} (\nabla T \cdot \vec{E}) \vec{E}^* - \frac{1}{2} \varepsilon_m \alpha \left| \vec{E} \right|^2 \nabla T \right] \tag{2.11}$$

where α and β are the linear and volumetric coefficients of thermal expansion and T is the absolute temperature. The additional drag force from the electro-thermally induced flow can be found by solving the Navier-Stokes equations and using equation (2.11) as the volume force term.

2.1.3 Random Brownian force

Brownian motion is the random movement of particles suspended in a fluid [15]. Since water molecules move at random, a suspended particle receives a random number of impacts of random strength and direction in any short period of time. Water molecules are about 1 nm in

size; therefore particles such as viruses are small enough to feel the effects of these impacts. Due to its random nature, no net movement results from these impacts.

Brownian motion is modeled mathematically by the random walk theorem [17]. It will follow a Gaussian profile with a displacement given by

$$\Delta x = \sqrt{\frac{k_B T}{3\pi r_p \eta_m} t} \tag{2.12}$$

where k_B is Boltzman's constant and t is the period of observation. In order to move an isolated particle in a deterministic manner during this period, the displacement due to the dielectrophoretic force should be greater than Δx. As is shown by the simulation results presented in section 5.6, the magnitude of the dielectrophoretic forces that can be generated by our lab-on-a-chip is large enough that random displacement due to Brownian motion won't hinder our ability to manipulate particles.

3.0 3D LAB-ON-A-CHIP FOR DIELECTROPHORESIS

In this chapter, we present a detailed description of our dielectrophoresis-based lab-on-a-chip design. The first section contains a brief summary of the 3D integration process. This is followed by a description how we take advantage of features inherent to 3D integration to create dense electrode arrays and areas for containing fluids. We also give a detailed description of the electronics integrated on the chip.

3.1 FABRICATION OF 3D INTEGRATED CIRCUITS

The lab-on-a-chip we designed is fabricated using MIT Lincoln Labs 3D, 0.18 um, silicon-on-insulator (SOI) technology [21]. For this integrated circuit process, three dimensional circuit structures are formed by transferring and interconnecting conventional silicon wafers in a vertically tiered fashion, as seen in the illustration of figure 3.1. The 3D integration process begins with the fabrication of three fully depleted SOI tiers. The handle silicon is removed from the second tier. After which, it is turned upside down and bonded to the first wafer tier using a low-temperature oxide bond. The third tier is transferred to the two-level stack using the same processing steps as for the second tier. Three-dimensional vias are etched through the oxide layers of the tiers and filled with tungsten, allowing for vertical interconnect between tiers. Each

tier has three metal layers that can be used for routing and can support the creation of transistors. Appendix A shows a cross-sectional view of the layers present in the final assembly.

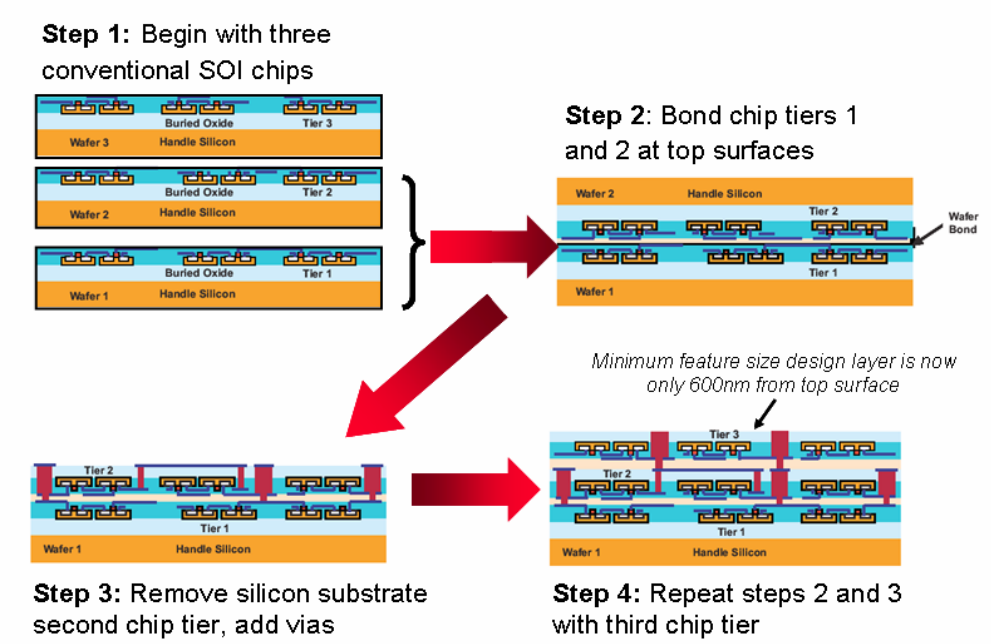

Figure 3.1. Fabrication procedures MIT Lincoln Labs 0.18 µm 3D integrated circuit process (used with permission) [20]

Since the topmost tier is assembled upside down with respect to its normal orientation, the polysilicon layer that is normally towards the bottom surface of a chip is in close proximity to the top outside surface. For integrated circuit processes, polysilicon is the design layer used to create geometries with the minimum size supported by the technology since this is the material that is used to make the gates of the MOS transistors. The minimum feature size that can be fabricated with the technology used in this design is 180 nm. For this reason, we used the polysilicon layer on that tier to design the dielectrophoresis electrodes for our lab-on-a-chip.

3.2 DESIGN OF 3D LAB-ON-A-CHIP

The three-dimensional chip stack, depicted by figure 3.2, is organized as follows: the topmost chip tier, tier three, is the location of a microfluidic trench used for containment of the aqueous medium and the polysilicon electrode array. The voltage on each electrode is individually driven by analog circuitry located on the middle tier. The bottom tier, tier one, contains the digital circuits that are used for control of the waveform on each electrode.

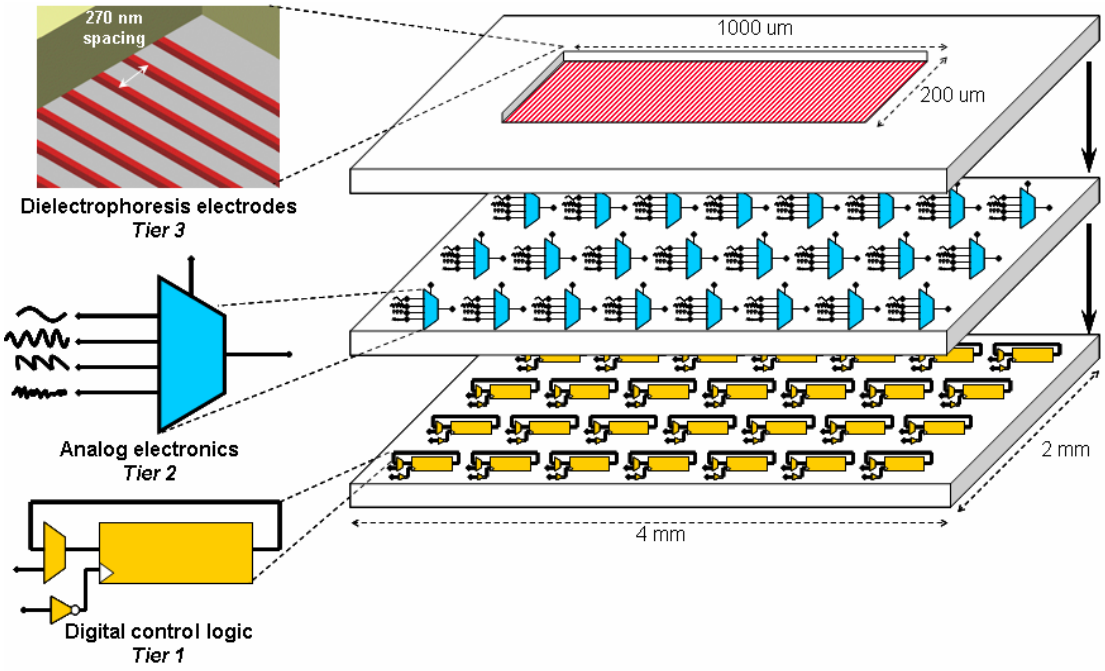

Figure 3.2. Organization of 3D lab-on-a-chip. The top chip tier is used for the dielectrophoresis electrode array. The electrodes are driven by analog circuitry on the middle tier, while the bottom tier contains digital control logic and memory.

3.2.1 Design of Dielectrophoresis Electrodes

The central components of the lab-on-a-chip design are the microfluidic trench and dielectrophoresis electrode array. The design of these components begins by designating a large

area as an electrical contact pad and then chemically etching away the top-level metal layer. A cross-sectional view of the lab-on-a-chip after the completion of this step is shown in figure 3.3. This etch has a two-fold purpose. First, etching away the metal leaves a 2 µm deep trench on top of the chip. This trench is what is used for containment of the aqueous solution and particles. Second, it puts the bottom surface of that trench only 600 nm away from the polysilicon layer, separated by a thin layer of silicon-dioxide (SiO_2).

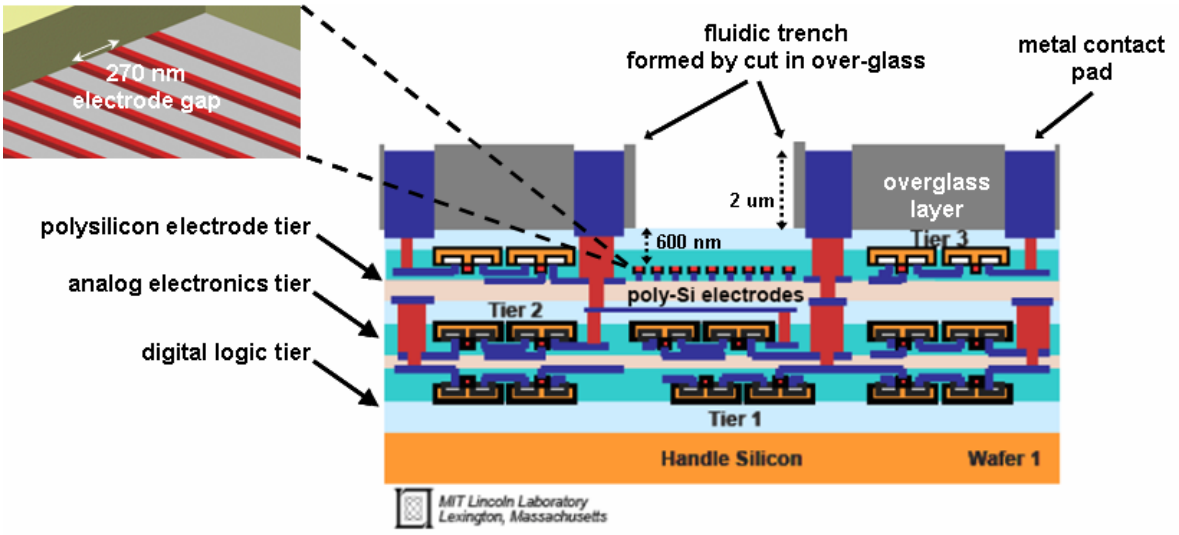

Figure 3.3. Cross-sectional view of 3D lab-on-a-chip. Displayed on each tier are the active silicon and interconnect layers. The center over-glass cut is how the on-chip fludic trenches are formed [20].

We designated a 1,000 um x 200 µm area for the microfluidic trench. A linear array of 2,048 electrodes, each being 180 nm wide and 200 µm long, is able to fit under this region. The design rules of the fabrication technology limit the electrode gap spacing to 270 nm, resulting in an array with a center to center pitch of 450 nm.

Using the polysilicon layer to form electrodes yields several advantages that would not have been possible if a conventional integrated circuit process was used. First, having sub-surface electrodes simplifies the problem of on-chip fluid containment by eliminating the need to

build additional retaining structures in a post-processing step. Second, the resulting electrode array is much denser than the arrays used in current labs-on-chips implemented in integrated circuit technologies. Those systems are only able to form trapping electrodes using the top metal layers normally reserved for bonding pads and result in a minimum gap spacing that is in the 2 μm to 20 μm range [22, 23]. Having a finer electrode pitch yields a higher degree of selectivity when manipulating submicron size particles. As seen in equation (2.4), the volume of the particle is directly proportional to the magnitude of the dielectrophoretic force. Therefore, as the size of the particle decreases, the magnitude of the dielectrophoretic force exerted on it decreases. In order to capture a nanometer scale particle, the strength of the electric field surrounding it needs to be very strong [24]. This can be accomplished by minimizing the array pitch, since the electric field magnitude is inversely proportional to the electrode gap spacing.

3.2.2 Design of Analog Electronics

The electronic design of the chip is based on an array of 2,048 analog multiplexers that select the waveform on each of the 2,048 electrodes. These multiplexers connect the electrodes to external waveform generators. This architecture provides flexibility for post-fabrication experimentation because the design is not limited by the generation of on-chip waveforms.

Figure 3.4 shows the schematic for one of the analog multiplexers. A CMOS transmission-gate implementation was used because of its relatively small area and low power consumption. Routing constraints limited the maximum number of multiplexer inputs to four.

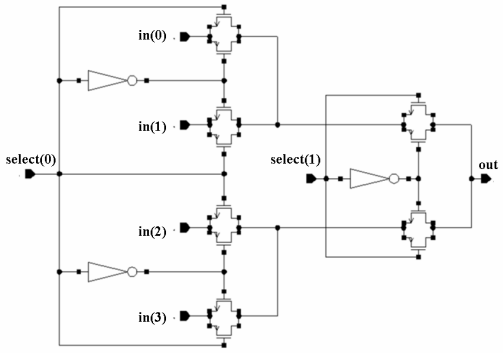

Figure 3.4 Analog multiplexer circuit used to control voltage waveform on each electrode

3.2.3 Design of Digital Electronics

The block diagram in figure 3.5 shows how the analog selector circuits are controlled digitally. The select input of each analog mux is driven by a 2-bit wide, 4-bit deep circular shift register. The shift registers have two modes, load and circulate. In order to minimize the number of I/O pins necessary for loading, the output of the last register in each row is used as the input to the subsequent row. The output of the final register in the chain is buffered and connected to an output pad so that it can be observed for post-fabrication diagnostics. Once the time sequenced pattern for each row has been initialized and the chip placed into circulation mode, the signal on the electrode can switch between one of four analog inputs on every clock cycle.

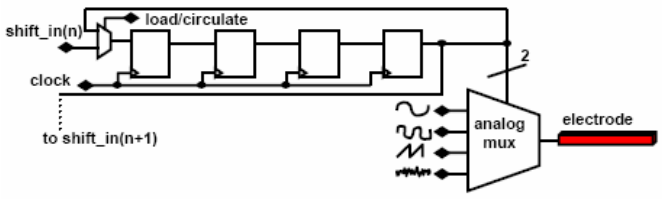

Figure 3.5 Block diagram of digital circuits used to control each analog multiplexer.

Since such a large number of registers are required to control the electrode array, we designed a balanced clock tree to ensure synchronization of the control logic. We also made the

decision to distribute the inverted clock signal through the tree instead of generating it locally within each master-slave flip-flop. This tradeoff doubles the size of our clock tree but results in an overall area savings by eliminating one inverter cell for each bit of each shift register.

Figure 3.6 shows a superposition of the VLSI layout of all three chip-tiers. The layout was done using the *Cadence Virtuoso* GDSII editor. Because the design is in a 3D process, there were additional floorplanning and routing issues that are not present in the design of conventional chips. For this 3D process, all three-dimensional vias made between chip tiers have to be exactly 1.75 µm x 1.75 µm in area with a minimum spacing of 5.8 µm between contacts. This is quite large in size when compared to the minimum feature size of the technology, 0.18 µm. As seen in the layer map (appendix A), an additional area penalty is taken on tier 2 and tier 3 when 3D contacts have to be made. These contacts cut through the entire tier, blocking any area that could be used for transistors or metal-layer routing in that region. Tier 1 has the most available area for placement and routing because 3D vias do not pass all the way through it (appendix A). This led to the decision to place the chip components that consumes the most area, the digital logic cells, on that bottom tier.

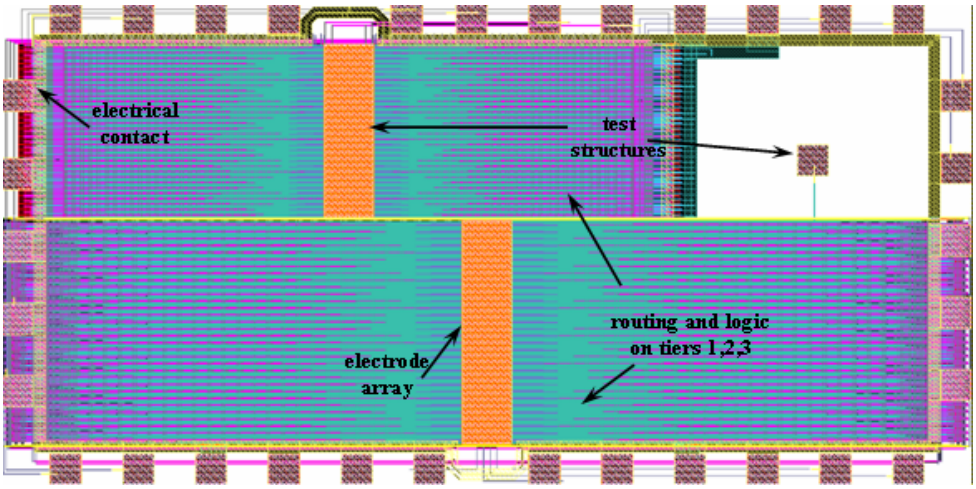

Figure 3.6 VLSI layout of lab-on-a-chip. Layers on all three chip tiers shown.

An additional benefit of placing all of the digital circuits on the bottom tier is that it locates them at a further distance from the trench area. The digital section of the chip consumes the most power and consequently produces the most heat. This extra heat makes the problem joule heating of the fluid worse, generating even more unwanted Stokes forces on the particles.

For the final step of the design process, we used *Mentor Graphics Calibre* physical verification toolset to perform layout versus schematic and design rule checks. Calibre was selected because its supports hierarchical extractions of netlists from layouts, which are less computationally intensive to verify than flat netlists.

4.0 OPTICAL DETECTION OF TRAPPED PARTICLES

Lab-on-a-chip microsystems have to have a method in place for collecting data about the analysis taking place on the chip. However, since virus particles are below the diffraction limit of conventional microscopes, detecting them on lab-on-a-chip devices is a difficult problem. Electron microscopy is needed to actually "see" them, which is both costly and impractical.

Currently, the most common approach to the problem of detection is to fluorescently mark the particles being manipulated [25,26,27,28,29]. The use of fluorescence is suitable for testing the functionality lab-on-a-chip prototypes, but not for actual use in biomedical applications. Using fluorescence requires extra preparation and handling of the samples prior to testing. Also, in the case of analyzing living organisms, having to alter their biochemistry is undesirable. Other researchers [22] have proposed integrating photodetectors directly onto the labs-on-chips. This technique does not scale well and requires that the chip is designed using a process that can support on-chip photodetectors.

In this chapter we present a technique we developed to detect the presence of particles on lab-on-a-chips. Our approach is to use dielectrophoresis to arrange particles into periodic striped patterns that resemble the form of a diffractive phase grating. This allows the particles to be sensed using conventional lab optics without having to alter their optical properties.

4.1 DIFFRACTION GRATING THEORY

A diffraction grating (figure 4.1) is a reflecting or transparent element whose optical properties are periodically modulated [30]. They are commonly realized by a collection of diffracting elements separated by a distance comparable to the wavelength of light being used. When light is incident on a grating, constructive interference effects cause the light to be both transmitted and reflected in discrete directions, known as diffraction orders.

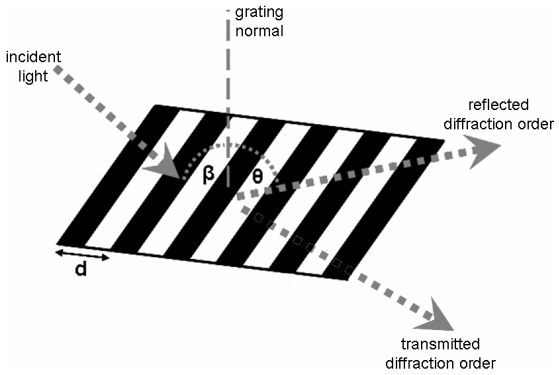

Figure 4.1 Diffraction Grating in which incident light is transmitted and reflected into diffracted orders at an angle of θ to the normal plane .

Diffractive elements placed at a pitch d with light of wavelength λ incident at angle β, is described by the grating equation:

$$m\lambda = d\left(\sin\theta + \sin\beta\right) \qquad (m = 1, 2, 3, \ldots) \qquad (4.1)$$

where θ is the diffracted angle at which constructive interference occurs in the m^{th} diffractive order. Equation (4.1) also shows that only diffraction orders for which $\lambda < \frac{2d}{m}$ are physically realizable. When light diffracts off a grating, both transmitted and reflected rays exist for a given order. However, the relative intensity between the reflected and transmitted orders will vary depending on whether or not it is designed to primarily be a transmission or reflection grating.

In addition to creating diffraction gratings by using periodic patterns of transparent and opaque regions, gratings can be produced by modulating the refractive index of a substrate. Gratings of this type are referred to as "phase gratings"[48]. Either rigorous coupled wave analysis (RCWA) or modal analysis is generally required to accurately model the diffraction efficiency of a phase grating [49]. However, the first order efficiency (η_g) of a phase grating can be estimated by[48]:

$$\eta_g = sin^2\left[\frac{\pi \cdot \Delta n_g \cdot w}{\lambda cos(\beta)}\right] \tag{4.2}$$

Equation (4.2) is the result of a simplified coupled-wave analysis that includes only the 0^{th} and 1^{st} diffraction orders and shows that the intensity of the diffracted light depends on the average index modulation contrast (Δn_g) and the distance light has to travel through the substrate that is being modulated (w).

4.2 SENSING PARTICLES USING DIFFRACTIVE OPTICS

Figure 4.2(a) shows a situation in which particles are randomly distributed throughout the fluidic containment area of our lab-on-a-chip. If the chip is programmed to create a pattern of alternating electric field maxima and minima, particles will be attracted to the maxima and arranged into a periodic form, similar to what is seen in figure 4.2(b). Once the system has reached a steady state and all of the particles are trapped by dielectrophoresis, the index of refraction along the bottom surface of the trench will be periodically modulated. We approximate this variation of optical properties as a diffraction grating. The diffraction efficiency of this particle-based grating can be measured by shining monochromatic light on it

and then measuring the intensity of the reflected diffraction orders. This measurement allows us to correlate that efficiency to the presence of particles in the medium, thereby alleviating the need for submicron detection techniques. Sensing nanoparticles in this manner also has the benefit of not requiring the use of biological-labeling techniques.

The most straightforward detection scheme that can be realized using this technique is a simple determination of whether or not particles are present in the sample under test. Since the periodicity of trapped particles is programmable, the angle at which to expect diffracted orders for a given incident wavelength can be predetermined by using equation (4.1). If light can be detected in those diffraction orders, it can be concluded that the particles are present in the sample.

It is also possible to perform a more sophisticated analysis of the sample by measuring the intensity of the diffracted orders. From equation (4.2), we can see that if the average contrast, incident angle and wavelength are all fixed, then the magnitude of the intensity can be used to create a mapping between it and the size of the contrast regions that were created by the particles.

The simulations in the next chapter demonstrate how the lab-on-a-chip can be used to arrange particles into the form of a diffraction grating and present a quantitative analysis of its detection capabilities.

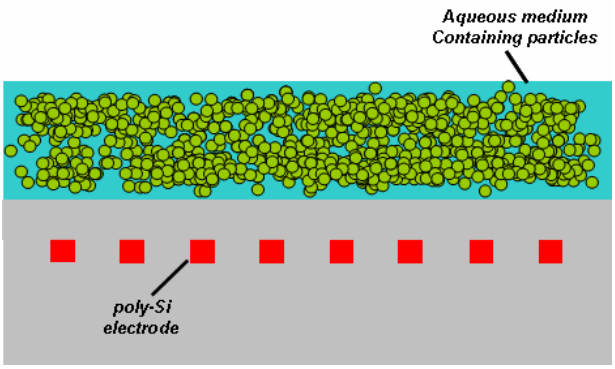

Figure 4.2(a) Random distribution of particles contained within the fluidic trench of lab-on-a-chip

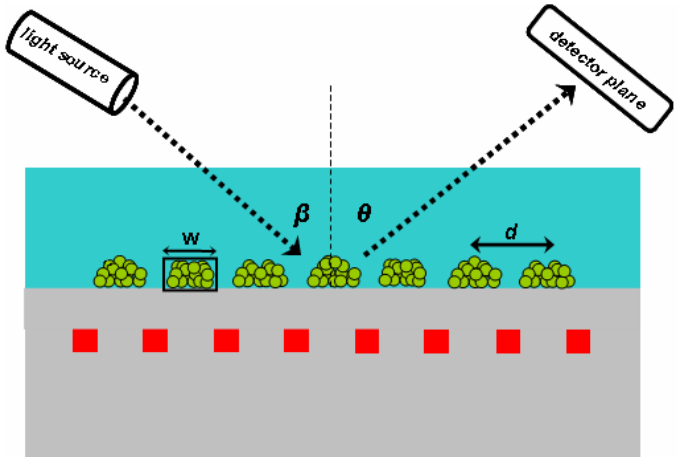

Figure 4.2(b) Particles arranged by dielectrophoresis into a periodic grating pattern that can be detected using conventional diffractive optics

5.0 SIMULATION STUDY OF 3D LAB-ON-A-CHIP

In this chapter we present the results of a simulation study to characterize the functionality of our lab-on-a-chip. The model particle for our study is the KSHV virion. Simulating lab-on-a-chip devices is an arduous task because they operate in many physical domains, some of which are tightly coupled to others (e.g. electrical, , optical, thermal, fluidic, etc.). Therefore, the simulation requires the use of many design automation tools.

Our simulation flow (figure 5.1) begins with the electronic design of the digital and analog components in the *Cadence* environment. We use the electrode geometries from this design and the results of *HSPICE* electrical simulations as inputs to both the *Ansoft* and *COMSOL* finite element solvers. *Ansoft* is used to compute the dielectrophoretic force vectors while the multi-domain coupling capabilities of *COMSOL* are used to calculate the thermally-induced fluid motion that results from the interaction between the electrostatic, thermal and fluidic domains. The resulting fluid velocity profile and the electrical force vectors are used to observe the movement of the virus particles in a custom discrete-time simulator written in *Matlab*. Finally, the optical characteristics of the steady-state arrangement of particles are analyzed using the *RSOFT DiffractMOD* package. We present each of these steps in detail in the following sections.

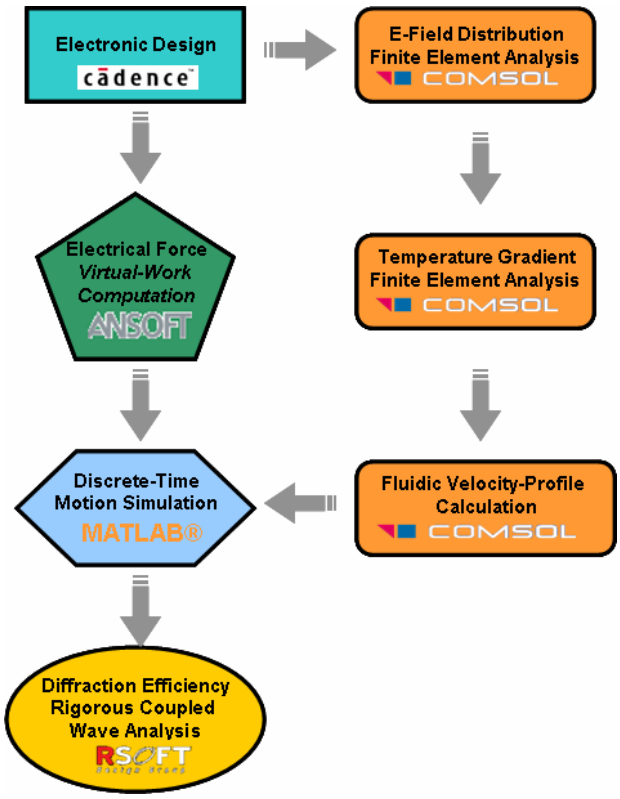

Figure 5.1 Simulation flow used to model behavior of 3D lab-on-a-chip

5.1 SIMULATIONS OF THE ELECTRONICS

The waveforms of figures 5.2 and 5.3 show the results of analog circuit simulations using *Synopsys HSPICE*. Figure 5.2 shows the result of four analog multiplexers each selecting from waveforms of 3MHz, 1MHz, 250 kHz and DC onto four of the electrodes. The shift registers that control each of the multiplexers select lines share a common clock signal. From this simulation, we can see that the analog multiplexers are able to pass voltage waveforms without distortion. The circular shift registers are switching the signals on the electrodes at a clock frequency of 125 kHz. Further simulations of netlists extracted from the GDSII layouts show

that the maximum switching frequency at which the clock tree and registers still operate reliably is 250 MHz.

Figure 5.3 shows the results of an AC analysis of all 2,048 analog multiplexers and electrodes. For this simulation, all of the electrodes in the array were connected to the same input source and the output on one of the electrodes is observed. The voltage magnitude on the electrodes drop off by -3db at a frequency of 42 MHz. The large fanout of the multiplexer input nodes along with the capacitive coupling between neighboring electrodes on the outputs limit the frequency response. External input frequencies above 42 MHz will most likely be too attenuated to produce a strong enough electric field inside of the fluidic containment area to perform dielectrophoresis.

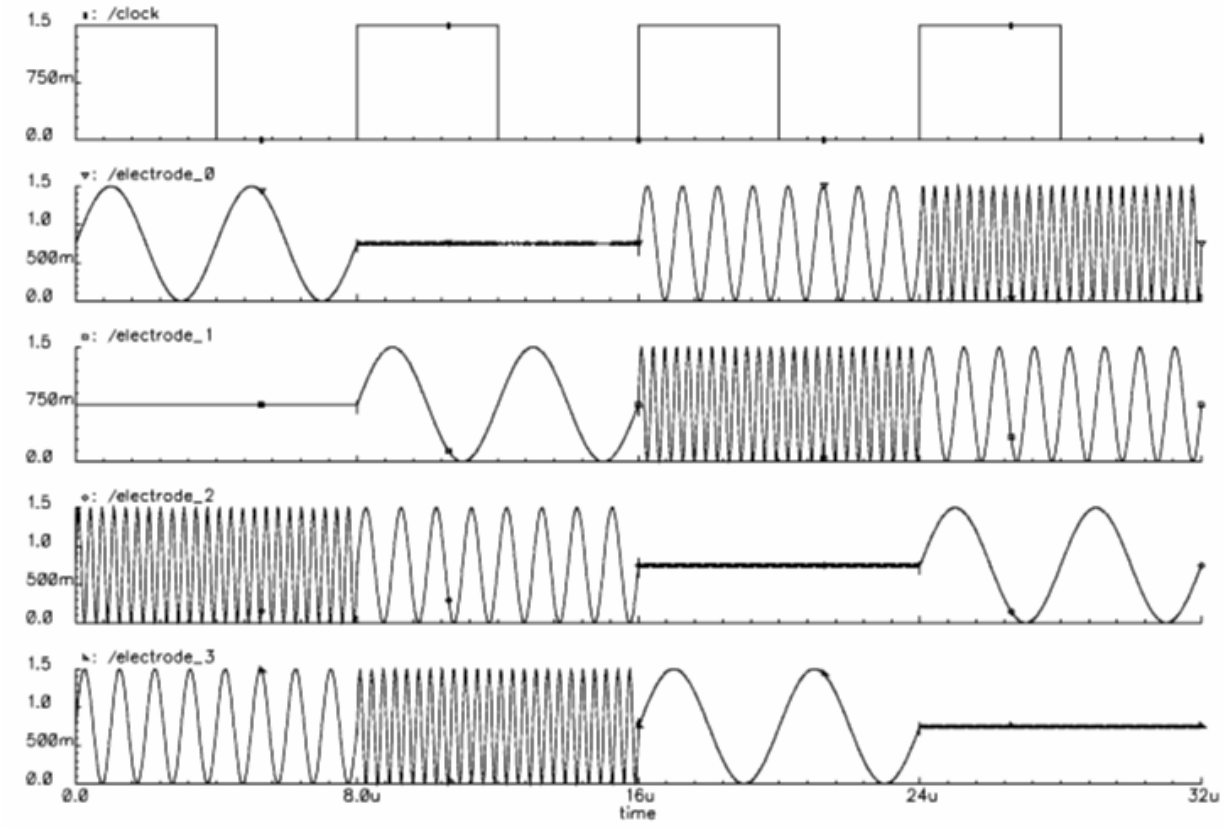

Figure 5.2 Waveforms of four 4:1 analog multiplexers switching the waveform on four electrodes at a clock frequency of 125 kHz

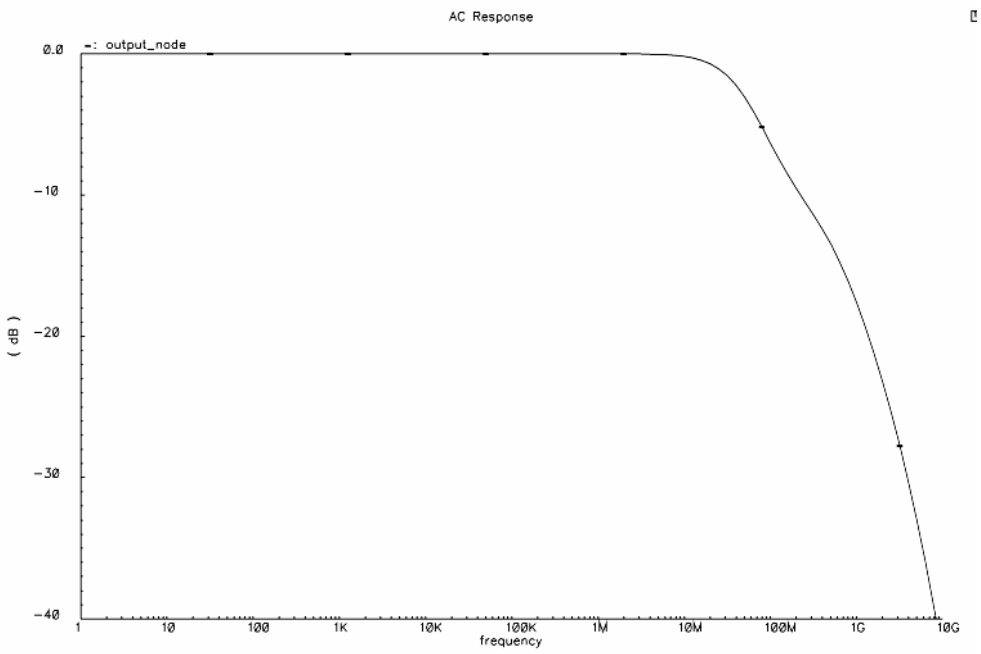

Figure 5.3 Frequency response of electrodes. Large fanout of multiplexer input nodes and capacitive coupling of neighboring electrodes results in a -3dB frequency of 42 MHz.

Table 5.1 summarizes the average power consumption of the lab-on-a-chip. The power consumed is primarily due to the clock tree and array of shift registers. The analog frequencies commonly used for dielectrophoresis are relatively low (kHz to low MHz). Therefore, as can be seen in the table, the power consumption of the chip is expected to be fairly small

Table 5.1 Average power consumption of 3D lab-on-a-chip

Clock Frequency	Average Power
25 kHz	330 μW
250 kHz	646 μW
2.5 MHz	3.36 mW
25 MHz	183 mW
250 MHz	1.73 W

From the simulations presented in this section we learn what voltage waveforms can be placed on the electrodes. In the next section, we use this information to perform a finite element analysis of the dielectrophoresis fields.

5.2 FINITE ELEMENT ANALYSIS OF DIELECTROPHORESIS FIELDS

Figure 5.4 shows the results of a 2D *COMSOL* finite element analysis of an electric field created inside of the trench by the electrodes. The conductivities and permittivities of the oxide layer and polysilicon electrodes are assigned values that reflect their material properties. The boundary condition at the top of the trench is set to be a grounded reference plane. Grounding the top surface of the fluid containment area both increases the magnitude of the intensity gradient (∇E_{RMS}^2) and results in more distinctly shaped electric field peaks and valleys. The electrode in the center of figure 5.4 is assigned a voltage of 1.5 V, while the remaining electrodes are grounded. This configuration creates an electric field maximum above the center electrode. The

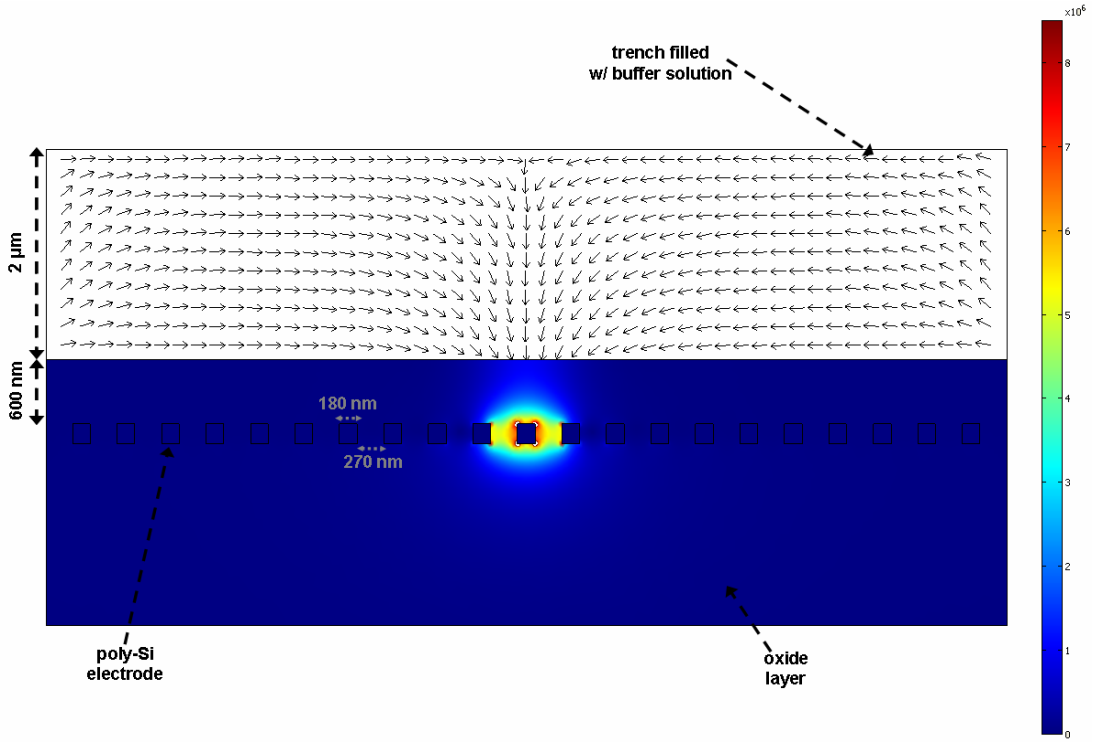

Figure 5.4 Electric field with single maximum. All electrodes except for centermost are grounded. Center electrode set to 1.5 V. Arrows show direction of intensity gradient.

arrows in figure 5.4 show the direction of the ∇E_{RMS}^2 term. The force vector $\vec{F}_{DEP}$ will be directed along these same paths in the case of particles undergoing positive dielectrophoresis, trapping

them in the region above the center electrode. Figure 5.5 is a plot from the same simulation with the scale adjusted so that electric field can be seen within the trench but not around the electrodes. The magnitude of the electric field at the oxide/fluid interface is 5.3×10^4 Vm^{-1}. This shows that even though the electrodes are separated from the fluidic medium by an insulating dielectric, the separation distance is small enough to support the creation of considerable electric fields within the trench.

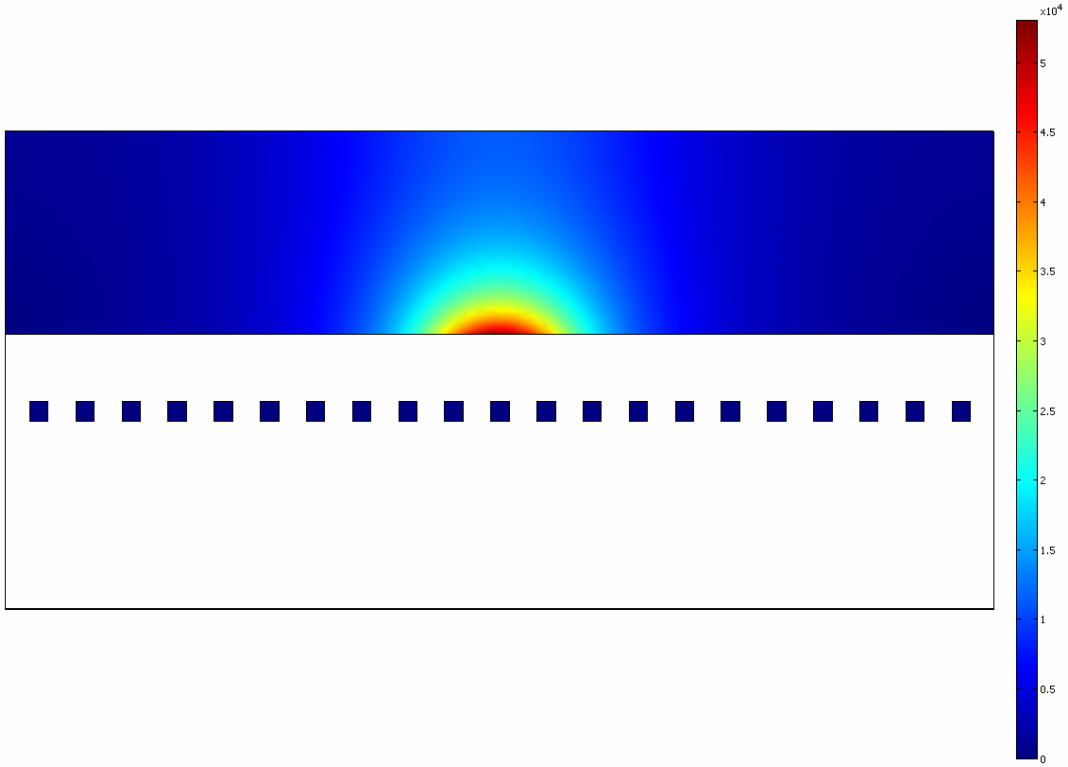

Figure 5.5 Profile of single-maximum electric field in center of trench area. Electric field magnitude at oxide-fluid interface above the center electrode is 5.3×10^4 Vm^{-1}.

Figure 5.6 shows the results of another 2D analysis in which each of the electrodes alternate between 1.5 V and ground. This electrode configuration in turn creates a pattern of alternating minima and maxima along the bottom surface of the trench. Particles undergoing dielectrophoresis in this case will be trapped along the bottom surface in a similar periodic form. The center-to-center pitch of the trapping points is 900 nm. This simulation is an example of an

electric field profile that can be used to create the particle-based grating structures discussed in section 4.2 and is the basis of the optical simulations presented in section 5.7.

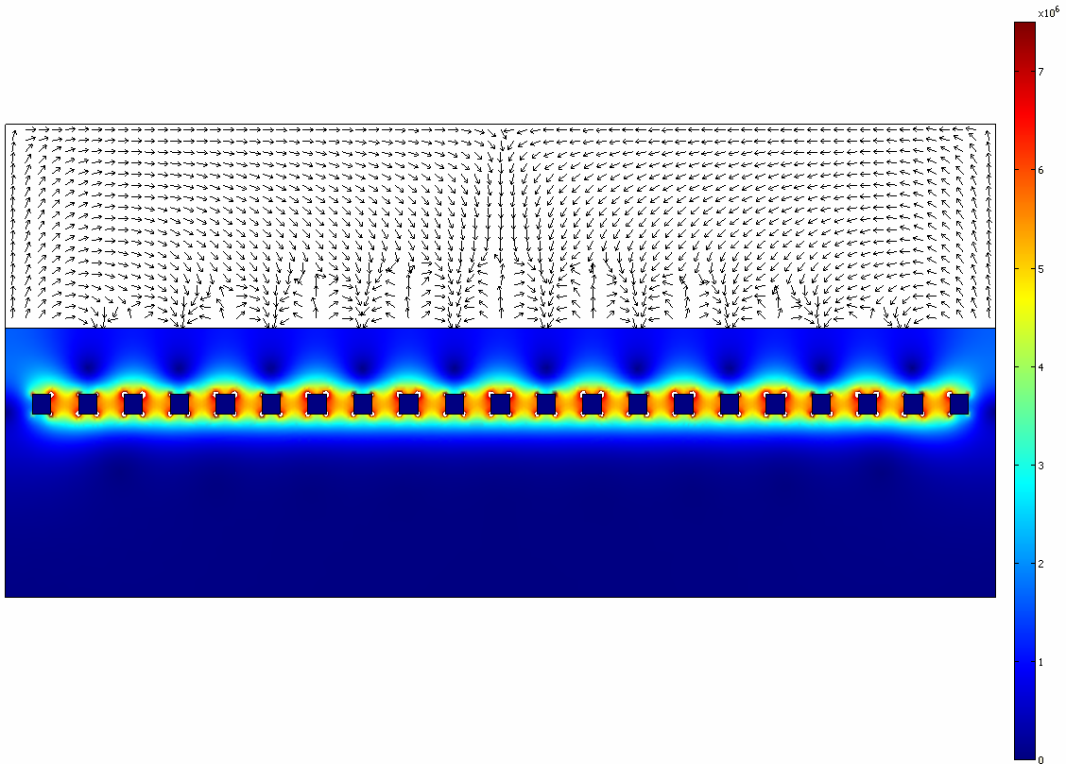

Figure 5.6 Alternating electric field minima and maxima created along bottom surface of trench by alternating voltages on neighboring electrodes between 1.5 V and ground. Arrows show direction of intensity gradient.

The simulations shown in figures 5.7(a) – 5.7(c) demonstrate how the electrodes can be time-sequenced to deterministically move particles. The sequence begins by creating a single electric field minima in the center of the trench (figure 5.7(a)), trapping particles in that area. For these simulations, the electrodes were configured to create electric field minima because negative dielectrophoresis is the most stable way to trap a particle [12]. Figures 5.7(b) and 5.7(c) show how the electrodes can be progressively activated in a shift-register fashion to create moving traps that the particles will follow. The amount of time it takes to complete this sequence depends on the velocity of the particles, which is examined in the simulations of section 5.6.

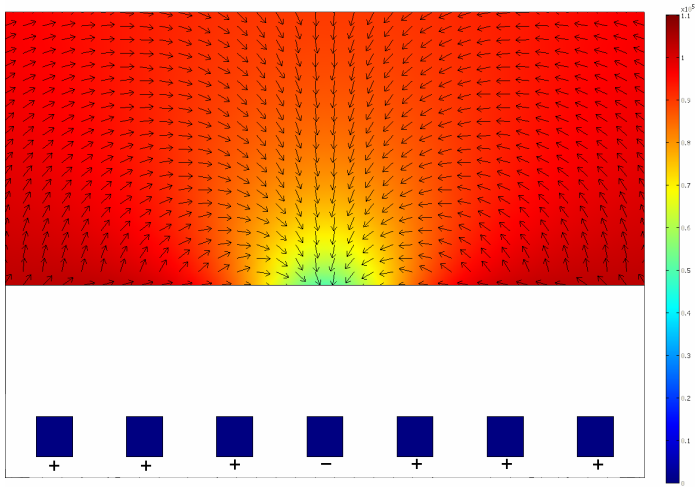

Figure 5.7(a). The Single negative dielectrophoresis trap in center will attract particles to the region above it. The arrows show direction of dielectrophoretic force vector. Electrode polarity annotated on bottom of plot.

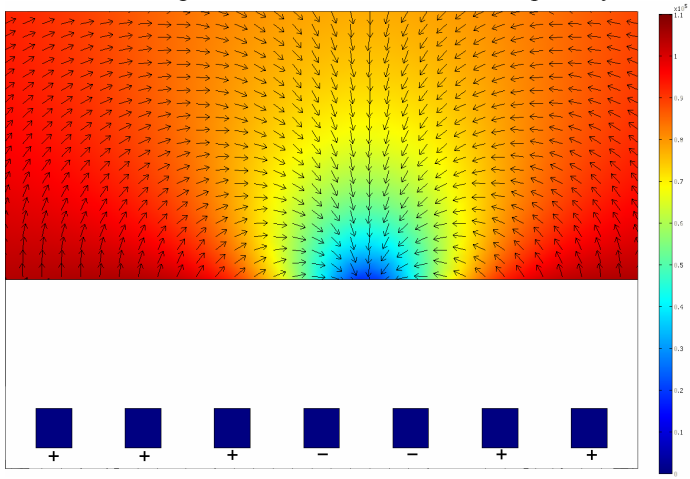

Figure 5.7(b). The change in electrodes polarity causes the location of the electric field minima to change

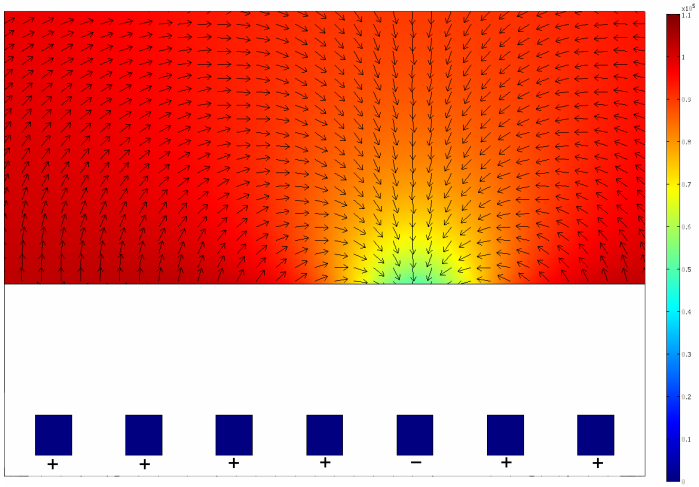

Figure 5.7(c). The particles new steady-state position shifted over 450 nm to the right by time sequencing the electrode polarities in a shift-register fashion.

For the electric field simulations presented in this section, the reference plane at the top of the trench is immersed in the medium and since buffer solutions used to contain biological media are usually conductive, joule heating of the fluid can occur. Joule heating of the aqueous medium will result in a thermally induced fluid flow that will exert additional drag force on the manipulated particles. We examine these factors in the following sections.

5.3 FINITE ELEMENT ANALYSIS OF TEMPERATURE GRADIENTS

The combination of an intense electric field inside of a conductive medium results in joule heating [14]. Heat is generated by power that is dissipated within the trench area. The volumetric power dissipation is given by the equation [14]:

$$W_m = \sigma_m |E|^2 \quad \left(W \cdot m^{-3}\right) \tag{5.1}$$

Figure 5.8 shows the temperature distribution resulting from the electric field profile shown in figure 5.7(a). This simulation is done using the *COMSOL* heat transfer finite element solver. For this analysis, the nominal temperature of the medium is set to 300 K, the thermal conductivity of the KCL buffer solution [32] is 0.61 $W \cdot m^{-1} \cdot K^{-1}$ and the expression for W_m is used as the heat source. The density and heat capacity of the solution are assigned values identical to water (1000 $kg \cdot m^{-3}$ and 4.72 $kJ \cdot kg^{-1} \cdot K^{-1}$). The temperature distribution varies from 300.000 K to 300.003 K. Since the temperature does not vary much, the magnitude of the electro-thermal forces associated with this gradient will be small. This temperature profile is used in the next section to calculate the velocity of the thermally induced fluid motion.

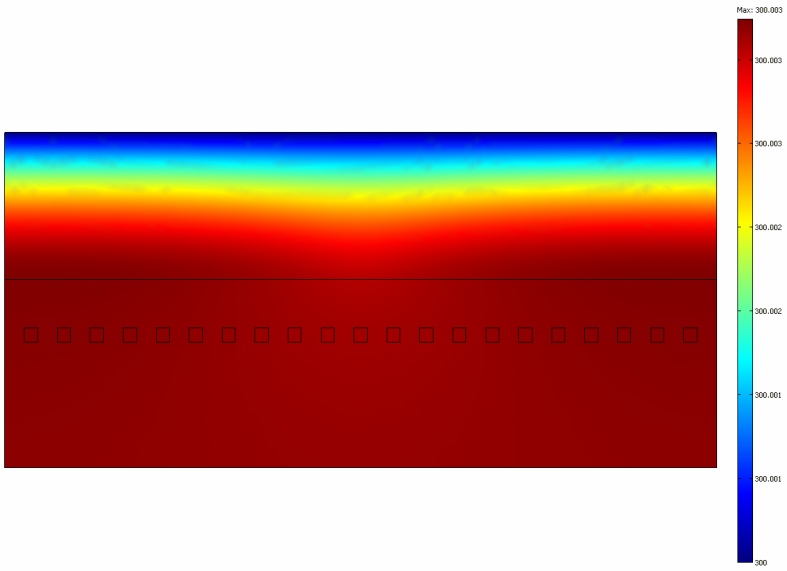

Figure 5.8 Temperature variations due to joule heating of fluid immersing the reference plane

5.4 CALCULATION OF FLUID VELOCITY PROFILE

The temperature field shown in figure 5.8 generates gradients in σ_m and ε_m, giving rise to an electrical body force on the fluid and resulting in additional drag force on the particles. Figure 5.9 shows the direction of $F_{thermal}$ in this case. In order to capture a profile of the stirring motion this force induces in the medium, the Navier-Stokes equations have to be solved with $F_{thermal}$ as the volume force term. However, since the profile presented in this section is the result of a DC electric field we can simplify the model with an approximation. At low frequencies, the coulombic force dominates the thermally induced fluid motion. Therefore, the magnitude of the fluid velocity (v_{max}) can be approximated by the equation [17]:

$$v_{max} \approx 5 \times 10^{-4} \frac{\varepsilon_m \sigma_m V_e^{\,4}}{k_m \eta_m d_e} \left| \frac{1}{\sigma_m} \frac{\partial \sigma_m}{\partial T} \right| \tag{5.2}$$

where k_m is the thermal conductivity of the medium, d_e is the distance from the electric field peak, V_e is the voltage difference across the electrodes (in our case V_e is adjusted to account for the reduction of the electric field by the oxide layer) and $\left|\frac{1}{\sigma_m}\frac{\partial \sigma_m}{\partial T}\right| \approx 0.02K^{-1}$ for electrolytic solutions [17].

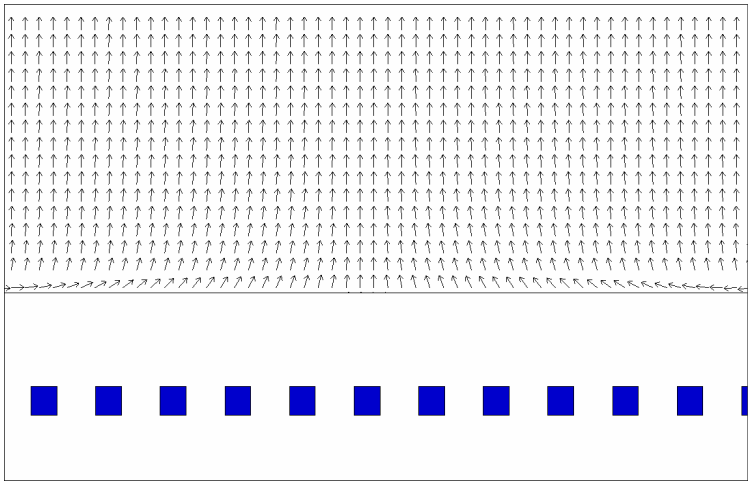

Figure 5.9 Direction of electro-thermal force vector ($\boldsymbol{F_{thermal}}$) within the trench area

Theoretically this expression goes to infinity as $d_e \rightarrow 0$. However, equation (5.2) has been shown to agree with finite element calculations if d_e is set to a value that is approximately equal to the length of the gradient [17], which is on the order of *1* μm in this simulation. This approximation results in a maximum fluid velocity of $1\text{x}10^{-15}$ μm·s^{-1} in the direction of $F_{thermal}$. The simulation results presented in section 5.6 show that the velocity of the particles due to dielectrophoresis is many orders of magnitude greater that this thermally induced fluid velocity. Therefore, the additional drag force exerted by this flow does not significantly alter the motion of the particles.

5.5 VIRTUAL-WORK CALCULATION OF ELECTRICAL FORCES

While the expression for $\vec{F}_{DEP}$ given in equation (2.4) provides insight on how the particle interacts with its surrounding medium, it is a derivation of force based on the assumption that the electric field does not change significantly over the length of the particle [12]. This assumption is not valid when the radius of the particle is on the same order of magnitude as the gap spacing between trapping electrodes. When they are similar in dimension, as is the case for the simulations presented in this chapter, a more rigorous analysis is required. Therefore, we used a simulator with the capability to accurately predict values of the dielectrophoretic force vector using the virtual-work method [36]. In order to predict how a KSHV virion will respond to dielectrophoresis using this method, we first have to model its electrical properties.

5.5.1 Electrical Modeling of KSHV Particles

Previous research has shown the use of dielectrophoresis to manipulate herpes simplex virions [27,33,34,35]. Since KSHV is very similar in its physical structure to HSV, we used the same electrical model as in reference [27] for this work. Figure 5.10 shows the physical structure of the virion, or complete virus particle, is modeled as two concentric shells, as depicted by figure. The outside layer is an approximately 20 nm thick insulating shell, referred to as the lipid bilayer. That shell encloses a thick conductive gel called the tegument. The lipid bilayer is modeled as having a surface conductance of 10 nSm^{-1} and permittivity of $10\varepsilon_0$. The electrical properties of the tegument are modeled as having a conductivity of 0.005 Sm^{-1} and permittivity of $70\varepsilon_0$. The physiological buffer used in this model is a KCL solution with conductivity of 0.1

Sm^{-1} and permittivity of $78\varepsilon_0$. Using a medium that is more conductive than the virions ensures that the particles will undergo negative dielectrophoresis at low frequencies.

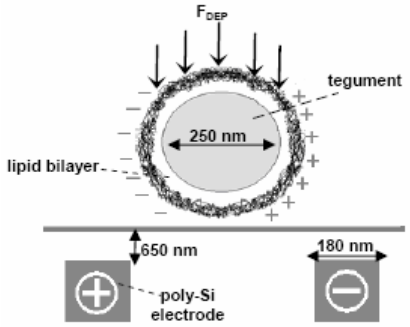

Figure 5.10 KSHV virion modeled as two concentric shells. The outer layer, the lipid bilayer, is an insulating shell that surrounds a conductive inner core, the tegument.

5.5.2 Virtual Work Calculation of Dielectrophoretic Force Vector

Figure 5.11 shows the model used in the *Ansoft Maxwell* finite-element solver to calculate the electrical force exerted on the particle. The KSHV shell-model, polysilicon electrodes, oxide layers and fluidic medium are all included in the model. Because of the presence of the particle, the model is no longer infinitely symmetric in the third dimension (x-axis in figure 5.11), making it necessary to do the simulations in 3D. The simulations are done by traversing the KSHV model in 250 nm increments throughout every point in the medium, re-meshing and resolving the model at each step. Since the electric field is uniform across the third dimension, there is no dielectrophoretic force along that axis and the particle is not traversed there. In the case of the electric field profile shown in figure 5.7(a), the magnitude of the dielectrophoretic force ranges on the order of 10^{-14} N to 10^{-16} N, depending on its proximity to the electric field minima.

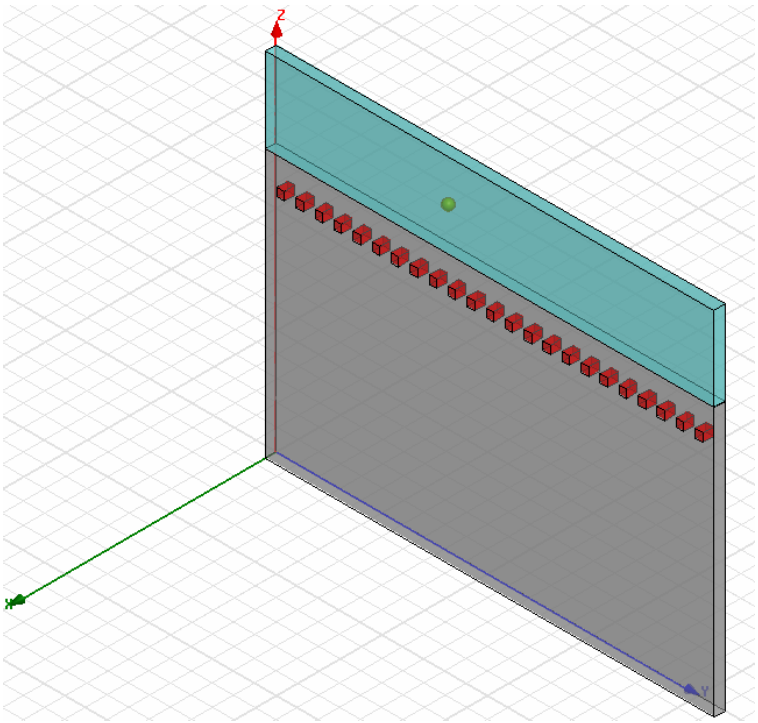

Figure 5.11 3D model used to calculate dielectrophoretic force vector using the virtual-work method

The virtual-work method is a very accurate approach to calculating electrical forces [36] but, it is computationally expensive. It takes 4 days running on a workstation with dual 2.2 GHz *Intel Xeon* processors and 4GB of RAM to evaluate the force vector at all 328 points in the space.

5.6 DISCRETE-TIME SIMULATION OF PARTICLE MOTION

We created a custom particle-motion simulator using *Matlab* that incorporates all of the forces described in chapter 2. These forces were either imported from simulation or calculated directly. Using a time-based simulator allows us to observe the movement of the virus models and the speed at which they travel.

The basis of the motion simulator are Newton's laws of motion, which in the case of a particle moving in our system can be written as

$$F_{ext} - F_{drag} = m_p \frac{dv_p}{dt} \tag{5.3}$$

where $F_{ext} = F_{DEP} + F_{brownian} + F_{thermal} + F_{buoyancy}$ and m_p is the mass of a KSHV virion. Solving for the velocity of the particle v_p by separation of variables gives

$$v_p = \left(v_p(0) - v_m - \frac{F_{ext}}{6\pi\eta_m r_p} \right) e^{-t/\tau_p} + v_m + \frac{F_{ext}}{6\pi\eta_m r_p} \tag{5.4}$$

$$\tau_p = m_p / 6\pi\eta_m r_p \tag{5.5}$$

The mass of a KSHV virion is $m_p \approx 3.3x10^{-19}\ kg$ [10], resulting in a time constant of $\tau_p \approx 158\ ps$. The typical observation period for dielectrophoresis of small particles is on the order of seconds [17], which is much greater than the time constant. Therefore, the acceleration terms in equation (5.4) can be neglected and the particle can be considered to move at its terminal velocity:

$$v_p = v_m + \frac{F_{ext}}{6\pi\eta_m r_p} \tag{5.4}$$

This is in agreement with what is mentioned in section 2.1.1 about inertia being negligible for particles with very low Reynolds numbers.

Figures 5.12(a) through 5.12(d) show the results of a motion simulation in which a large concentration of virions are randomly placed inside of the trench. The electric field profile used in this simulation is the same as the one shown in figure 5.6, the voltages on each of the electrodes alternate between 1.5 V DC and ground. Because the electric field does not vary along the axis parallel to the electrodes, this profile was extruded into the third dimension. Figure 5.12(a) shows the distribution of the particles at time t = 0 s. As seen in figure 5.12(d), the particles reach their steady-state by t = 16 s and remain trapped after that. The average velocity of the particles is approximately 0.12 $\mu m \cdot s^{-1}$ and their motion is not significantly affected by Brownian motion, joule heating or buoyancy effects.

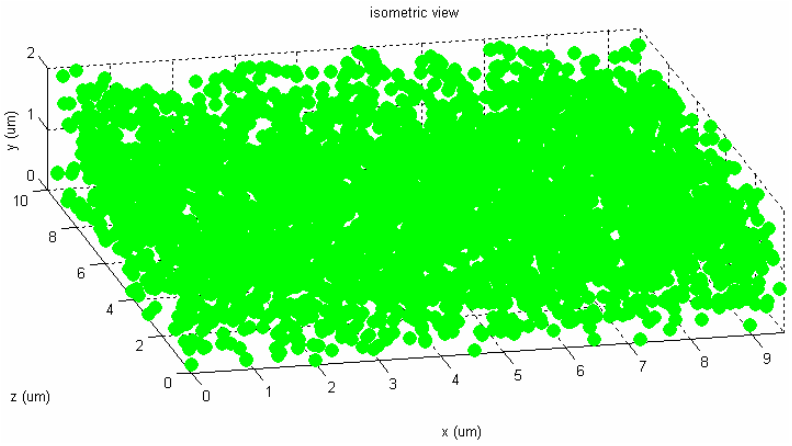

Figure 5.12(a) Initial position of particles (t = 0 s)

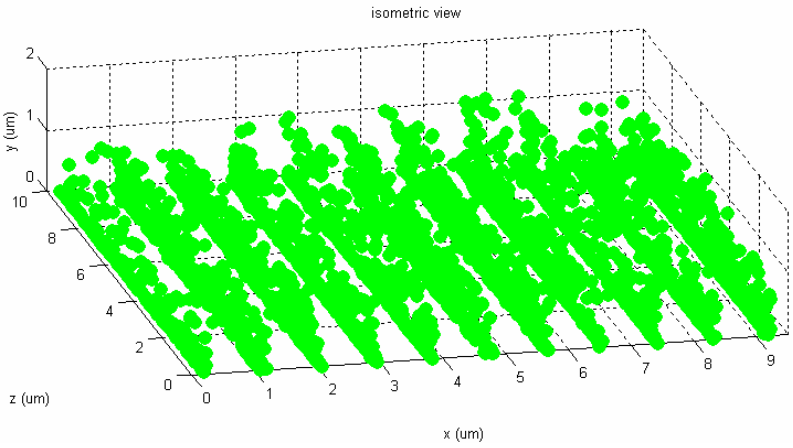

Figure 5.12(b) Distribution of particles at t = 7 s

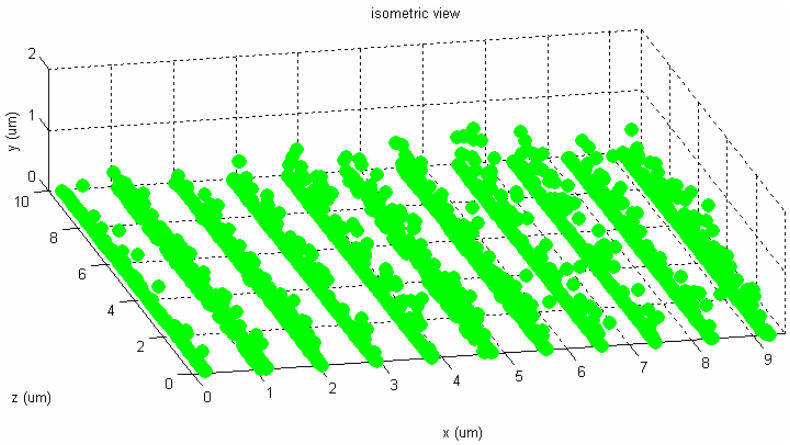

Figure 5.12(c) Distribution of particles at t = 11 s

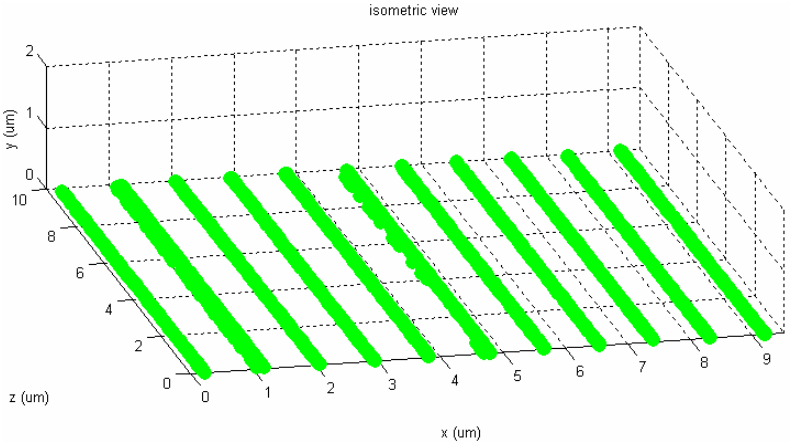

Figure 5.12(d) Distribution of particles for t > 16 s

The optical characteristics of the steady state arrangement of particles shown in figure 5.12(d) is analyzed in the next section.

5.7 RIGOROUS COUPLED WAVE ANALYSIS OF GRATINGS

In this section, we characterize the diffraction efficiency of the particle grating structures. Since the grating has a multi-layered profile, its optical characteristics are complex. Therfore, we performed a rigorous coupled wave analysis (RWCA) of the structure using the *RSOFT DiffractMOD* software package to accurately calculate efficiency. Figure 5.13 shows a cross-sectional view of the RSOFT model. The RWCA algorithm assumes the diffractive structure is infinitely periodic in one or more dimensions, so it only requires information about one period of the grating structure to calculate how the light diffracts, however figure 5.13 includes multiple periods for clarity.

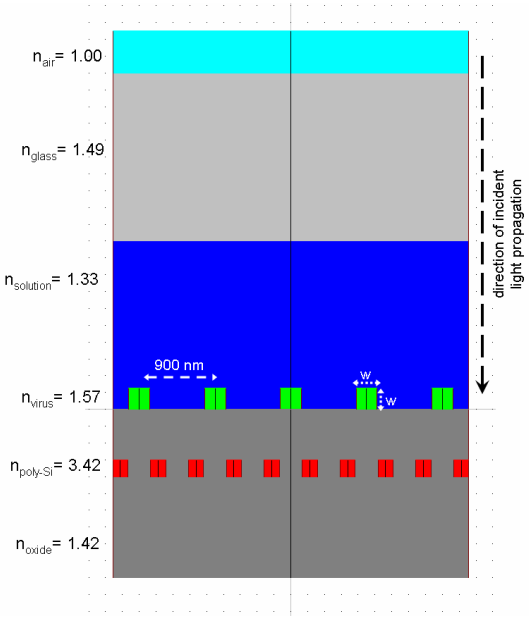

Figure 5.13 Multi-layered grating structure used in rigorous coupled wave analysis. The period of the trapped virus particles is set to 900 nm, while the index modulation depth, w, is varied. Indices of refraction for each layer annotated on left hand side of figure.

The incident light is a single-wavelength plane wave that propagates through layers representing air, the glass lid, the buffer solution, the chip oxide layers, polysilicon electrodes and trapped virus particles. The angle of incidence is 0^0 with respect to the normal plane of the trapped particles. Since the index of refraction for KSHV particles is not readily available, the value used in this model, n_{virus} = 1.57, is taken from a similar virus for which this data is published [37]. For the RWCA simulations presented in this chapter, the period of trapped particles is set to 900 nm, which corresponds with the electric field profile seen in figure 5.6 and used in the simulation of figure 5.12.

5.7.1 2D Diffractive Analysis

The first step of the analysis is the selection of the incident wavelength. For a 0^0 incident angle, the wavelength is bounded by equation (4.1) to $\lambda < \frac{d}{m}$. However, care must be taken not to select too short of a wavelength. This is demonstrated by the simulation results shown in figure 5.14(a). Figure 5.14(a) is a plot of reflected power, relative to the input power, versus the angle of observation. The discrete diffraction orders are annotated on the graph. For this simulation, the width of the trapped particle region is 250 nm and the incident wavelength is 200 nm. Such a short wavelength leads to multiple unwanted diffraction orders that disperse energy at very wide angles. Using ultraviolet light in this case also gives rise to reflected orders due diffraction off of the electrode array, because it too is a periodic modulation of the index of refraction. Both of these effects can be avoided by selecting a longer wavelength.

Figure 5.14(b) shows results from the same simulation with the incident wavelength changed to 500 nm. Only one diffraction order {-1, 1} due to the trapped particles can

physically exist at this wavelength. The reflected power of this order is 13.8% of the input power and is observed at an angle of 33.75^0. Since periodicity of the dielectrophoretic traps is a controlled variable, the existence of this order can be used as indicator of whether or not virus particles are present.

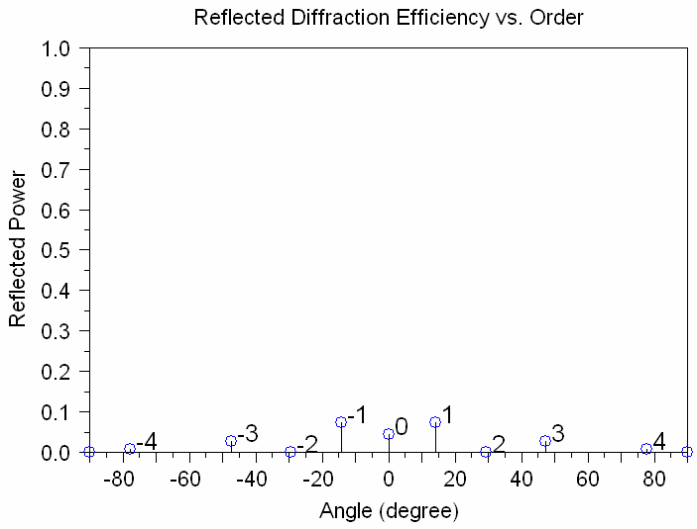

Figure 5.14(a) Reflected diffraction efficiency versus of observation angle for w = 250 nm and λ=200 nm. Multiple unwanted orders exist due to short wavelength and diffraction off of electrode array. Discrete diffraction order annotated on plot.

Figure 5.14(b) Reflected diffraction efficiency for w = 250 nm and λ=500 nm. Only one reflected order {-1,1} exists due diffraction off of trapped particles.

Figure 5.15 shows the results of multiple simulations in which the width of the cross-sectional area of the particles is varied. The diffraction efficiency gradually increases as with the area and reaches peak at $w \approx 400\ nm$. The maximum diameter of a KSHV particle will most likely be smaller than this peak. Therefore, if it is assumed the particles are trapped in a single-file line, the graphs of figure 5.15 can be used a tuning-curve to create a mapping between the average size of the trapped particles and diffraction efficiency.

This change in efficiency can be measured in a laboratory environment by observing the decrease in power at the 0^{th} order, which corresponds to light undergoing specular reflection. Likewise the increase in power of the {-1,1} reflected order can be detected.

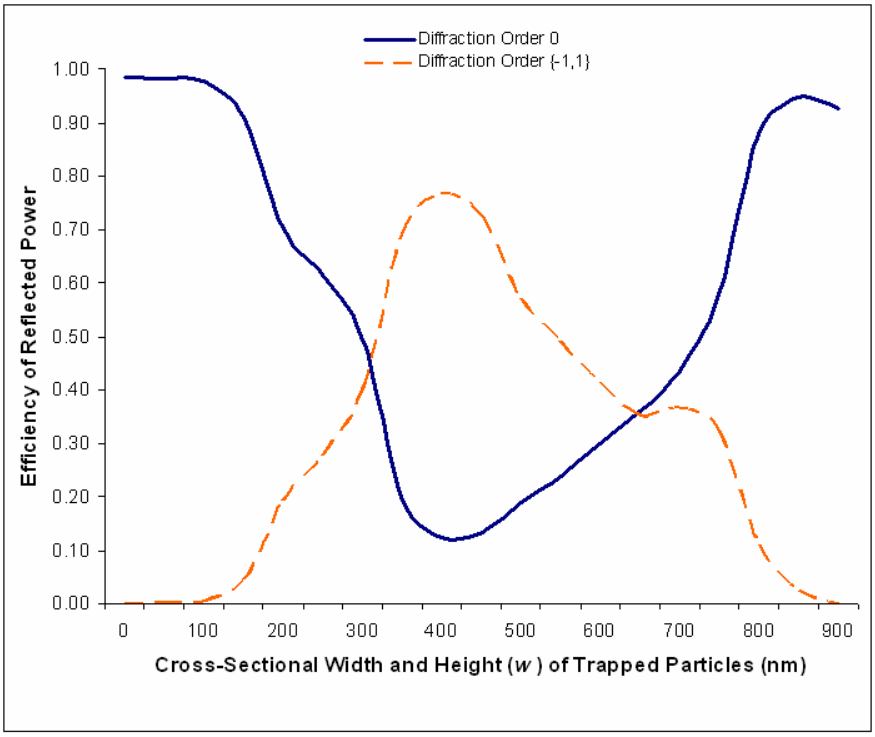

Figure 5.15 Reflected diffraction efficiency versus cross sectional area of trapped particle regions.

The simulations presented in this section are based on assumption that the optical model of figure 5.13 can be extruded infinitely into the third dimension. If the concentration of

particles in the buffer solution is low enough, this assumption is not valid. We examine this situation in the next section by performing 3D RWCA simulations.

5.7.2 3D Diffractive Analysis

In order to perform a 3D analysis, we used the same model of figure 5.13 and specified lengths for the third dimension. Because RWCA can only simulate structures that are infinitely periodic in all but one dimension, the change in particle concentration is modeled by varying the periodicity of particles along that third axis (z-axis). Figure 5.16 shows how the structure of the diffraction grating will be significantly changed depending on the concentration of particles in the solution. If the concentration is significantly low, then the particles will no longer form solid lines.

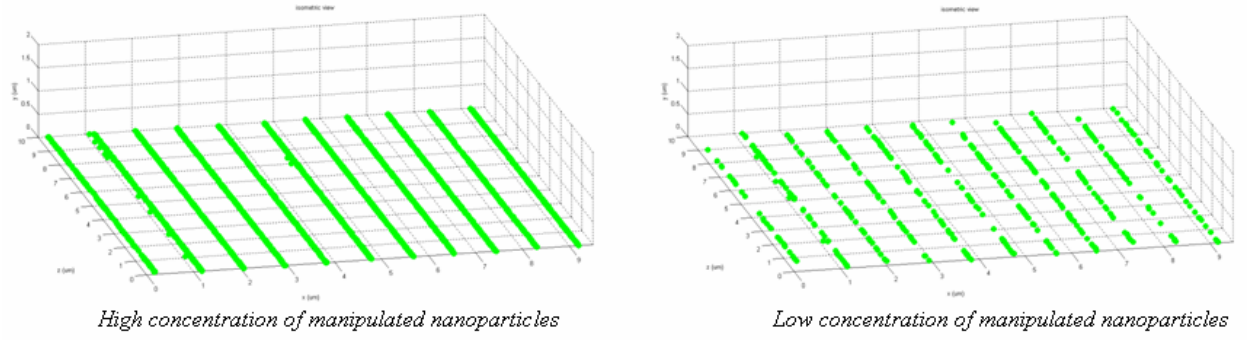

Figure 5.16 Depiction of the difference in the structure of the nanoparticle diffraction grating based on the concentration of particles

Figures 5.17(a) through 5.17(b) are grids that show reflected efficiency versus the diffraction order at which it is found. The scales are adjusted so that all the present orders can be seen. In the simulation of figure 5.17(a), $w = 250\ nm$, $\lambda = 500\ nm$ and the period of the particles on the z-axis is 0 nm. This corresponds exactly to the 2D example presented in figure 5.14(b). and only the (0,1), (0,0), (0,-1) diffraction orders are present. The periodicity of the particles

along the z-axis is increased to 571 nm and 800 nm in figures 5.17(b) and 5.17(c). These changes result in the existence of new diffraction orders that can be used to estimate particle concentration. For example, the change from the particles not being periodic along z to a periodicity 571 nm (5.17 (b)) resulted in the addition of the (-1,0), (1,0) orders to the diffraction pattern.

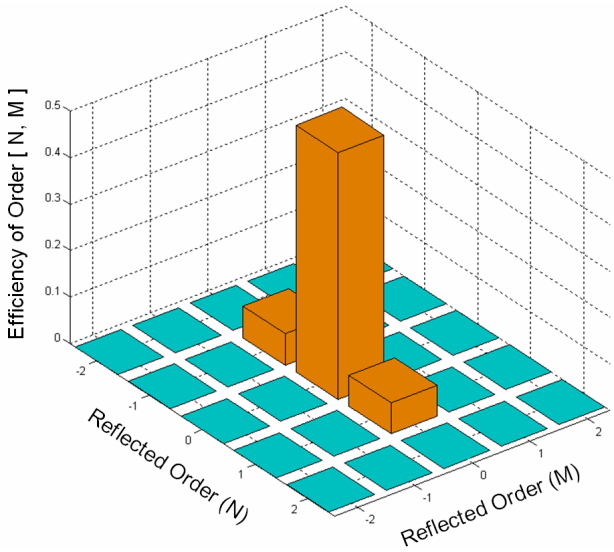

Figure 5.17(a). Diffraction order vs. efficiency for w=250 nm, λ=500 nm. Period of particles along z-axis is 0 nm.

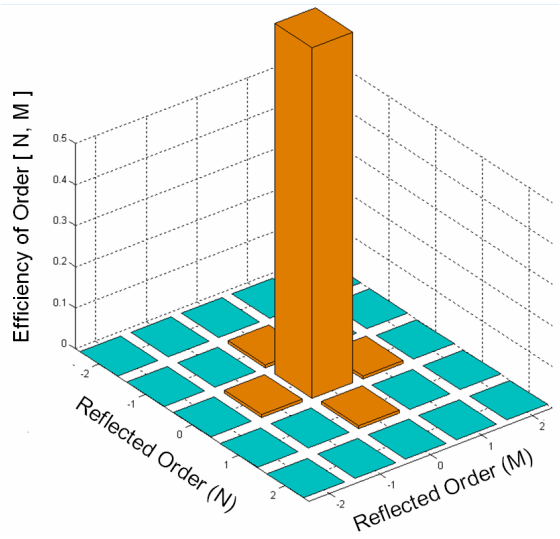

Figure 5.17(b). Periodicity of trapped particles along z-axis changed to 571 nm.

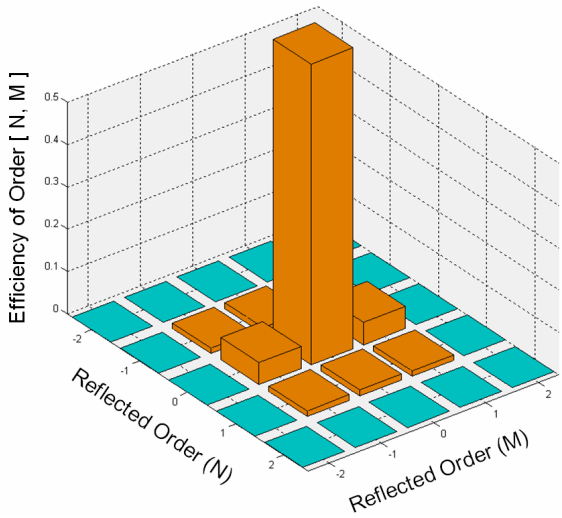

Figure 5.17(c). Periodicity of trapped particles along z-axis changed to 800 nm.

6.0 POST-FABRICATION PROCEDURES FOR 3D LAB-ON-A-CHIP

There are several post processing steps that will need to be completed after the chip has been fabricated and prior to testing its functionality. First, the top level metal will be etched away in order to form the microfluidic trenches used for solution containment. A lithographic mask will be used to coat the top surface of the chip with photoresist and the trench areas will be revealed by way of exposure to UV light. The top metal will be removed by using a wet chemical etch, with the oxide layer on the bottom and sidewalls of the trench acting as the etch stop.

If we find that the efficiency of the naturally reflected diffraction orders are too low, our next step will be to coat the bottom surface of the fluidic containment areas with a high-reflective dielectric thin-film. The deposition of such a thin-film would bring the reflectivity of the oxide surface within the 90% to ~100% range [38], greatly improving the signal-to-noise ratio of the measured intensity.

The chip will not be placed in an IC package, but will be affixed directly to a custom PCB with an epoxy. All 34 of the electrical I/O contacts will be made from the chip to the board using a manual wire bonder (See appendix B for complete chip pinout).

The final steps before testing the functionality of the chip will be to fill the on-chip trench with the aqueous medium and particles of interest. Current pressure-regulated microinjectors are capable of injecting and vacuuming volumes as small as femtoliters [XX]. Since the volume of the trench in our design is 400 picoliters, we will require the use such a microinjection system.

The microfluidic channel will then be sealed with a conductive glass lid that will be used as the reference plane.

6.1 TEST PLAN

One goal of labs-on-chips is to be able to integrate as many laboratory functions as possible onto one device. As the complexity of these chips increases, so does the number of things that can lead to their failure. Therefore, it is essential to have a thorough test plan for initial prototypes.

The first functional test we carry out will determine if the digital circuitry is alive and working. We will load the chain of shift registers with a pattern of alternating 1's and 0's. An output pad is connected to the output of the last register in the chain so that it can be observed on an oscilloscope. This pad will not be wire bonded to the PCB but will be probed using a micropositioner. If the same pattern that was initially loaded is observed on the output, then we will be able to conclude that the clock tree is functioning properly and that we are able to successfully write both 1's and 0's to each bit of each shift register.

The first test of the chips ability to manipulate particles will be done with latex spheres that are approximately 250 nm in diameter. We chose to experiment first with latex particles because they are easier to obtain and require less effort to handle than live virions. Manufactured particles also have less variation in size when compared to a sample of living organisms, therefore, the response of each particle to dielectrophoresis will be more predictable. Previous work [34] has shown that when spheres of this type and dimension are placed between out-of-phase electrodes in a KCL solution with a conductivity of 250 μSm^{-1}, they will experience positive dielectrophoresis at a frequency of 1 MHz. We will use this setup as our starting point.

If no movement is detected using these parameters, we will be able to sweep the frequency and/or adjust the conductivity of the KCL solution. We will avoid the need for electron microscopy to detect particle movements by fluorescently marking the spheres and observing collections of particles with an optical microscope.

The next experiment will measure the diffraction efficiency of the trapped particles. Figure 6.1 shows the setup that will be used to test the efficiency [30]. The monochromator will filter the desired wavelength from the light source and the collimator will then direct the beam towards the grating. The incident light will be polarized to help eliminate reflections from the fluidic medium on the chip and its glass lid. The light will then pass through an aperture, truncating the beam to a width that is appropriate for the grating. The diffracted orders will be converted to an electrical signal by the detector and after amplification, will be compared to a directly measured reference signal in order to evaluate the grating efficiency.

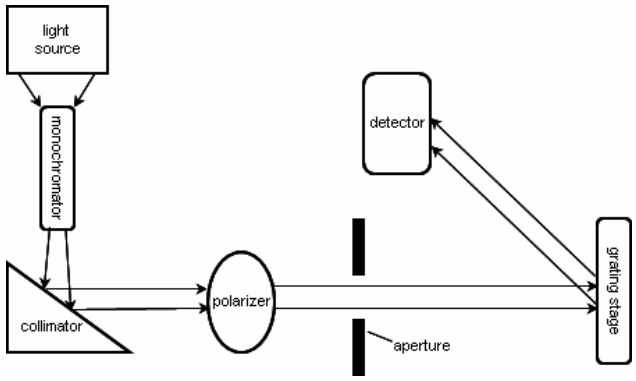

Figure 6.1 Setup for measuring diffraction efficiency of gratings

The final test will be a repetition of these experiments with KSHV virions. Experimental results [27] have shown that when HSV particles are placed in a mannitol solution of conductivity 0.005 Sm^{-1}, the particles will transition from undergoing positive to negative dielectrophoresis in the frequency in the range of 4 to 5 MHz, which is well within the operating

range of the circuitry on the 3D lab-on-a-chip. Once we reach this phase of testing, collaboration with molecular virologists will be required for assistance with the handling of KSHV particles.

7.0 SUMMARY

The design of a lab-on-a-chip in 3D integrated circuit technology is presented in this thesis. The main features of the chip are summarized by table 7.1. The lab-on-a-chip has the capabilities to manipulate nanometer scale particles by way of dielectrophoresis. We take advantage of features inherent to 3D chip-making technology to create an on-chip microfluidic trench with an extremely dense electrode array under it. In addition to the components necessary for dielectrophoresis, we also integrate analog and digital electronics onto the chip. We also demonstrate in this thesis a new technique for detecting manipulated particles by arranging them into diffraction grating structures. We verify the operation of the lab-on-a-chip by performing a simulation study of its capabilities to manipulate KSHV virus particles and have them optically detected. We also give a plan for the post-fabrication steps and testing procedures that will be done on the initial prototype devices.

Table 7.1 Summary of 3D lab-on-a-chip specifications

Technology	3D 0.18μm SOI
Power supply	1.5V
Chip area	2x4 mm^2
# of dielectrophoresis electrodes	2,048
Electrode width	180 nm
Electrode center-to-center pitch	450 nm

7.1 CONCLUSIONS

In this section, we present our conclusions about the lab-on-a-chip design, our optical detection scheme and the simulation flow we used. Our lab-on-a-chip is the first ever to be designed in 3D integrated circuit technology and clearly shows the benefits of doing so. With this technology, we were able to create the most dense electrode array ever to be designed in a CMOS compatible process. In addition, our design does not require cumbersome post-processing steps for creating on-chip microfluidic channels. Also, having the capability to directly integrate a large amount of digital and analog electronics on to the chip makes it tremendously flexible; allowing it to be adapted to many applications even after it has been fabricated. All of these features make 3D chip stacking technology a promising platform for lab-on-a-chip design.

The technique we developed for detecting small particles is especially well-suited for lab-on-a-chip devices. This method of sensing is not tied to the design we presented here; it can be utilized with any lab-on-a-chip that has the capabilities to arrange particles into a grating-like form. Also, our technique has the added benefit that it does not require extra preparation of the sample-under-test, which is highly undesirable in the case of biological particles. Our sensing mechanism has the additional benefit of being relatively inexpensive; the optical components needed to implement our scheme have a price that is comparable to the low-cost optics found in modern CD players.

Due to the multidisciplinary nature of our chip, we had to research the fields of biology, chemistry, optics, fluid mechanics, thermodynamics, electrostatics, and electronic design. The design of this chip is a reminder that very few, if any, microsystem designers are experts in all of these fields. Therefore, we realize that there is a need for CAD tools to help with the end-to-end design of such multi-domain mixed-signal microsystems. The current methodology is to use a

different tool for each domain present and then stitch together the results using an additional tool, in our case *Matlab*. This process is time consuming, and in some cases, inefficient and will need to be addressed when such technologies such as labs-on-chips become more widespread.

7.2 FUTURE WORK

The short-term future work associated with this thesis is the improvement of our simulation flow. The first of which is the modeling of the dielectrophoretic force. Some have suggested [39] modeling the particle as a multi-pole rather than dipole. This raises the question, would doing so strike enough balance in the computation time/accuracy tradeoff that we could eliminate timely virtual-work computations? Also, there are other forces in action that are not included in our models. For example, researchers have shown that there exists a particle to particle interaction force that causes pearl-like chaining of the particles [40]. There also exists an AC osmotic force on the fluid that is associated with the electrical double layer at the interface of the medium [17]. The temperature gradients cause dynamic changes in the viscosity and density of the medium. We have included a few secondary forces in this work (electro-thermal effect, Brownian motion and buoyancy) and have found them to be insignificant but, is the aggregate effect of all these minor forces enough to significantly change the motion of the particles? There are also limitations to the optical simulations we performed. We were restricted by the tools we used to simulating infinitely periodic diffractive structures. However in reality, if the concentration of the particles is relatively low, chances are each row of trapped particles will look somewhat different. If that is the case, will there still be some sort of diffraction pattern due to the particles that we can detect and does there exist an efficient way to simulate it?

In addition to our test plan (chapter 6), there are many other tests we can perform because of the flexibility of our design. We've essentially created a test-bed with the ability to perform multiple types of dielectrophoresis experiments. For example, we could carry out traveling wave dielectrophoresis [41], field-flow fractionation [42], or multi-frequency dielectrophoresis experiments [50]. One future possibility stemming from our work could be the characterization of the optical properties of virus particles. There is very little published information about properties such as the index of refraction of virus particles. Our chip could be used to initiate new research and lead to new types of optical biological sensors.

Finally, our long term goal is to find specific applications for our 3D lab-on-a-chip. For example, we could possibly develop a blood filtration device that is programmed to route "bad" particles in one direction and "good" particles in another. If we do further research on scaling down our particle detection method and develop a way to get that information on to the chip, we can implement much more elaborate systems. An example of this could be a wearable device that monitors a patient for a certain type of virus. Such a device could possibly use dielectrophoresis to attract viruses to certain locations, use the feedback from the sensor to do a sophisticated analysis of the viruses with its integrated microprocessor and then alert the patient that he needs to increase his medication dosage to a certain level or maybe even rush to the hospital! The future possibilities for microsystems like our 3D lab-on-a-chip are both numerous and promising.

APPENDIX A

3D INTEGRATED CIRCUIT PROCESS DESIGN LAYERS

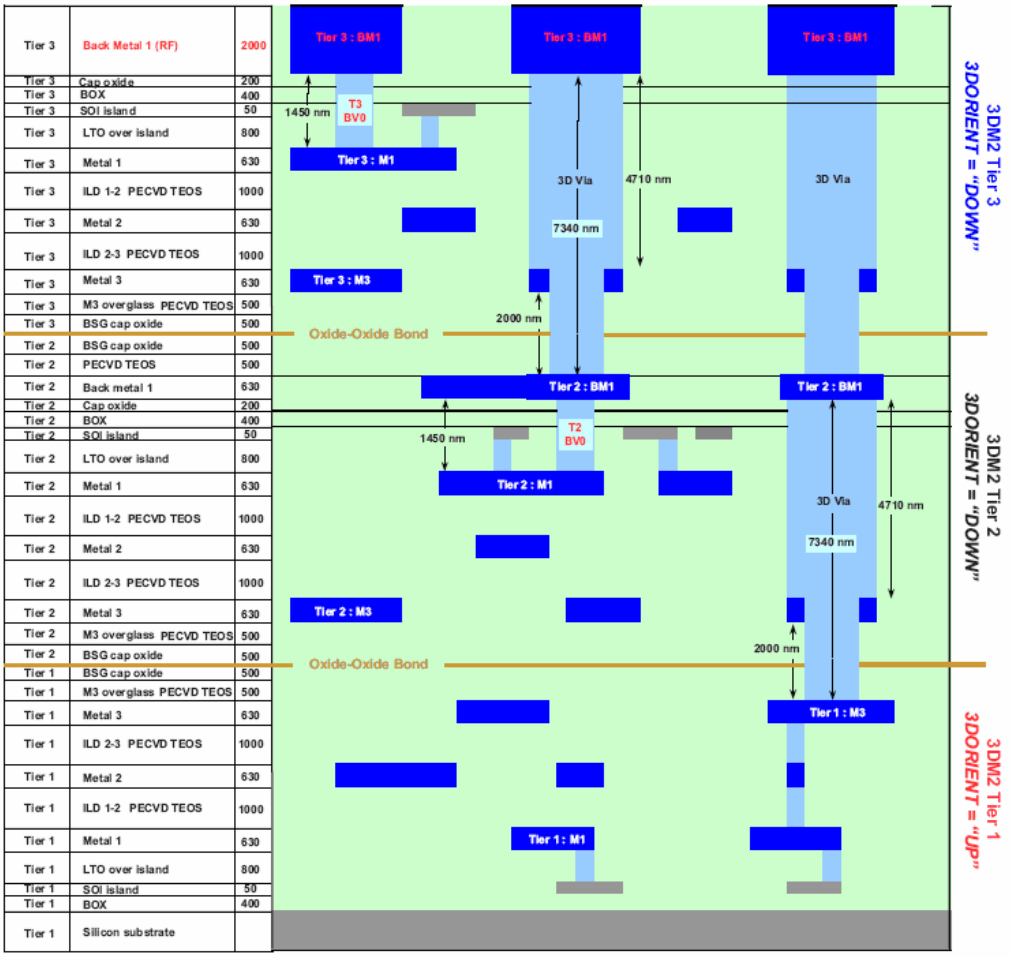

Figure A.1 Cross-section of design layers in Lincoln Labs 0.18 µm 3D SOI process [21]

APPENDIX B

3D LAB-ON-A-CHIP PINOUT

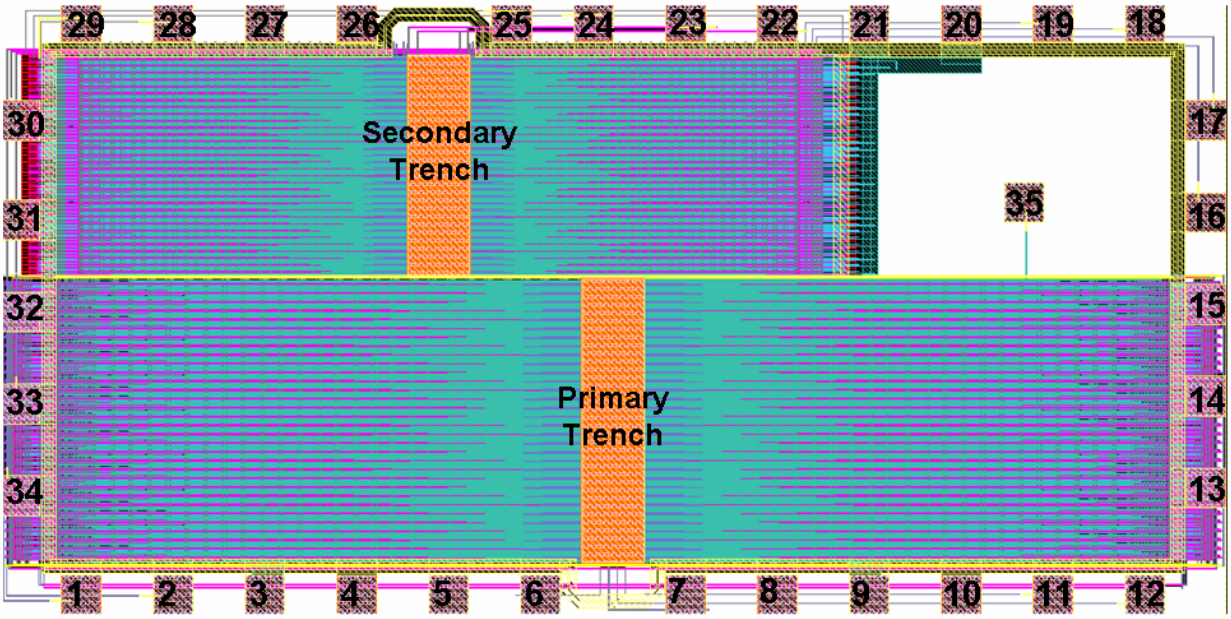

Figure B.1 Pinout of 3D Lab-on-a-chip

Table B.1 Listing of 3D lab-on-a-chip pin names and descriptions

Pin number	Name	Description
1	shift_in_0	1st bit of shift register daisy chain for primary trench
2	shift_in_1	2nd bit of shift register daisy chain for primary trench
3	vdd!	Global power supply
4	gnd!	Global ground reference
5	clk	Clock signal for primary trench
6	v_d	External analog waveform #4 for primary trench
7	v_b	External analog waveform #2 for primary trench
8	clk_b	Inverted clock signal for primary trench
9	vdd!	Global power supply
10	gnd!	Global ground reference
11	v_a	External analog waveform #1 for primary trench
12	v_c	External analog waveform #3 for primary trench
13	circulate	Circulate/load mode select for primary trench
14	gnd!	Global ground reference
15	vdd!	Global power supply
16	v_d1	External analog waveform #4 for secondary trench
17	v_b1	External analog waveform #2 for secondary trench
18	v_c1	External analog waveform #3 for secondary trench
19	v_a1	External analog waveform #1 for secondary trench
20	gnd!	Global ground reference
21	vdd!	Global power supply
22	clk_B_b	Inverted clock signal for secondary trench, mode B
23	clk_B	Clock signal for secondary trench, mode B
24	clk_A_b	Inverted clock signal for secondary trench, mode A
25	clk_A	Clock signal for secondary trench, mode A
26	gnd!	Global ground reference
27	vdd!	Global power supply
28	shift_in_1_tb	2nd bit of shift register daisy chain for secondary trench
29	shift_in_0_tb	1st bit of shift register daisy chain for secondary trench
30	mode_sel	Selects between mode A or mode B for secondary trench
31	vdd!	Global power supply
32	gnd!	Global ground reference
33	circulate_A	Circulate/load mode select for secondary trench, mode A
34	circulate_B	Circulate/load mode select for secondary trench, mode B
35	shift_out	*Output* of final bit in primary trench shift register chain

BIBLIOGRAPHY

1. Pohl, Herbert A. **"The Motion and Precipitation of Suspensoids in Divergent Electric Fields"**, J. Appl. Phys. 22, 869, 1951

2. Ghallab,Y.;Badawy,W., **"Sensing methods for dielectrophoresis phenomenon: From bulky instruments to lab-on-a-chip",** Circuits and Systems Magazine, IEEE, Vol.4, Iss.3, Third Quarter 2004, pp: 5- 15

3. Hughes, Michael Pycraft, **"AC electrokinetics: applications for nanotechnology",** Nanotechnology, 11, pp. 124-132 , 2000

4. Gambari R, Borgatti M, Altomare L, Manaresi N, Medoro G, Romani A, Tartagni M, Guerrieri R., **"Applications to cancer research of "lab-on-a-chip" devices based on dielectrophoresis(DEP)"**,Technol. Cancer Res. Treat. 2003 Feb;2(1):31-40

5. Huang, Y., Yang, J., Wang, X. B., Becker, F. F., Gascoyne, P. R., **"The removal of human breast cancer cells from hematopoietic CD34+ stem cells by dielectrophoretic field-flow-fractionation."** J Hematother Stem Cell Res., 1999, Oct;8(5):481-90.

6. Xu, C., Wang, Y., Cao, M., Lu, Z. **"Dielectrophoresis of Human Red Cells in Microchips."** Electrophoresis 20, 1829-31,1999.

7. Paul Yager, Thayne Edwards, Elain Fu, Kristen Helton, Kjell Nelson, Milton R. Tam and Bernhard H. Weigl **"Microfluidic diagnostic technologies for global public health",** Nature 442, 412-418(27 July 2006)

8. Chang, Y., Cesarman, E., Pessin, M. S., Lee, F., Culpepper, J., Knowles, D. M., and Moore, P. S.. **"Identification of herpesvirus-like DNA sequences in AIDS-associated Kaposi's sarcoma"**. Science. 265, 1865-69, (1994).

9. **http://en.wikipedia.org/wiki/Kaposi's_sarcoma-associated_herpesvirus**

10. Trus B.L., et al. **"Capsid structure of Kaposi's sarcoma-associated herpesvirus, a gammaherpesvirus, compared to those of an alphaherpesvirus,herpes simplex virus type 1, and a betaherpesvirus"**, cytomegalovirus. J. Virol. ,2001

11. Saliterman, S., **Fundamentals of BioMEMS and Medical Microdevices**, SPIE Press, 2006.

12. T.B. Jones, **Electromechanics of Particles**, Cambridge Univ. Press, 1995.

13. N. G. Green, A. Ramos, A. González, H. Morgan, and A. Castellanos, **"Fluid flow induced by nonuniform ac electric fields in electrolytes on Experimental measurements microelectrodes"**. I., Phys. Rev. E 61, 4011 (2000)

14. A Ramos, H Morgan, N G Green and A Castellanos, **"Ac electrokinetics: a review of forces in microelectrode structures"**, J. Phys. D: Appl. Phys. 31 2338-2353, 1998

15. Einstein, A.,**"The theory of the brownian movement" ,**Ann. der Physik, vol.17,1905

16. Green, NG and Ramos, A. and Morgan, H, **"AC electrokinetics: a survey of sub-micrometre particle dynamics",** J. Phys. D: Appl. Phys, vol. 33, 2000

17. Castellanos, A. and Ramos, A. and Gonzalez, A. and Green, N.G. and Morgan, H, **"Electrohydrodynamics and dielectrophoresis in microsystems: scaling laws",** Journal of Physics D: Applied Physics, vol 36, no. 20, 2003

18. E. M. Purcell, **"Life at low Reynolds number"**, American Journal of Physics Jan. 1977 Vol. 45 Issue 1, pp.3-11

19. Panton, Ronald, L. **Incompressible Flow,** third edition, Wiley, 2005.

20. Nicolas G. Green, Antonio Ramos, Antonio Gonzalez, Antonio Castellanos and Hywel Morgan, **"Electrothermally induced fluid flow on microelectrodes",** Journal of Electrostatics, Volume 53, Issue 2, August 2001, Pages 71-87.

21. MIT Lincoln Laboratory. **MITLL Low-Power FDSOI CMOS Process Design Guide**, September, 2006.

22. Manaresi, N.; Romani, A.; Medoro, G.; Altomare, L.; Leonardi, A.; Tartagni, M.; Guerrieri,R., **"A CMOS chip for individual cell manipulation and detection"** Solid-State Circuits, IEEE Journal of, Vol.38, Iss.12, Dec. 2003 Pages: 2297- 2305

23. Enteshari, A.; Jullien, G.A.; Yadid-Pecht, O.; Kaler, K.V.I.S. **"All CMOS low power platform for dielectrophoresis bio-analysis"** Solid-State Circuits Conference, 2005. ESSCIRC 2005,Vol.,Iss.,12-16,Sept.2005

24. Lifeng Zheng; Shengdong Li; Burke, P.J.; Brody, J.P., **"Towards single molecule manipulation with dielectrophoresis using nanoelectrodes"**,. IEEE-NANO. Vol.1, Iss., 12-14 Aug. 2003

25. Cui, L. and Zhang, T. and Morgan, H, **"Optical particle detection integrated in a dielectrophoretic lab-on-a-chip."** Journal of Micromechanics and Microengineering, vol. 12, no. 1,2002

26. Green, N. G., H. Morgan, and J. J. Milner. **"Manipulation and trapping of submicron bioparticles using dielectrophoresis"**. J. Biochem. Biophys. Methods. 35:89-102, 1997

27. Hughes, M. P., H. Morgan, F. J. Rixon, J. P. H. Burt, and R. Pethig.. **"Manipulation of herpes simplex virus type 1 by dielectrophoresis"**. Biochim. Biophys. Acta. 1425:119-126, 1998

28. Kentsch, J.; Durr, M.; Schnelle, T.; Gradl, G.; Muller, T.; Jager, M.; Normann, A.; Stelzle, **"Microdevices for separation, accumulation, and analysis of biological micro- and nanoparticles"** Nanobiotechnology, IEE Proceedings, Vol.150, Iss.2, 1 Nov. 2003

29. Bakewell, DJ and Morgan, H., **"Quantifying dielectrophoretic collections of sub-micron particles on microelectrodes",** Measurement Science and Technology, vol. 15, no.1, 2004

30. Palmer, Christopher. **Diffraction Grating Handbook**, 6th edition, Newport Corporation (2005).

31. Serway, Raymond. **Physics For Scientist and Engineers with Modern Physiscs**, 3rd edition, Saunders College Publishing, (1990)

32. Ramires M.L.V, Nieto de Castro C.A, **"Thermal Conductivity of Aqueous Potassium Chloride Solutions",** International Journal of Thermophysics, vol. 21, May 2000

33. Michael P. Hughes, Hywel Morgan and Frazer J. Rixon, **"Measuring the dielectric properties of herpes simplex virus type 1 virions with dielectrophoresis"**, Biochimica et Biophysica Acta, Volume 1571, Issue 1, 10 May 2002, Pages 1-8.

34. Morgan, H. and Hughes, M.P. and Green, N.G., **"Separation of Submicron Bioparticles by Dielectrophoresis",** Biophysical Journal, vol. 77, no. 1, 1999

35. Hughes, M.P. and Morgan, H. and Rixon, F.J., **"Dielectrophoretic manipulation and characterization of herpes simplex virus-1 capsids",** European Biophysics Journal, vol. 30, no. 4, 2001

36. J. L. Coulomb and G. Meunier, **"Finite element implementation of virtual work principle for magnetic or electric force and torque computation,"** IEEE Trans. Magn., vol. 20, pp. 1894–1896, Sept. 1984.

37. Oster, G., **"Two-Phase Formation In Solutions Of Tobacco Mosaic Virus and the Problem Of Long-Range Forces",** The Journal of General Physiology, vol. 33, no. 5, 1950

38. **http://en.wikipedia.org/wiki/Dielectric_mirror**

39. Jones, T.B., **"Basic Theory of Dielectrophoresis and Electrorotation",** IEEE Engineering In Medicine and Biology Magazine, vol. 33, 2003

40. Kadaksham, A.T.J. and Singh, P. and Aubry, N., **"Dielectrophoresis of nanoparticles",** Electrophoresis, vol. 25, no. 21-22, 2004

41. Hagedorn, R. and Fuhr, G. and Muller, T. and Gimsa, J., **"Traveling-wave dielectrophoresis of microparticles",** Electrophoresis, vol. 13, no. 1-2, 1992

42. Huang, Y. and Wang, XB and Becker, FF and Gascoyne, PR. **"Introducing dielectrophoresis as a new force field for field-flow fractionation",** Biophysical Journal, vol. 73, no. 2, 1997

43. Huang, Y. and Wang, XB and Becker, FF and Gascoyne, PR. **"Introducing dielectrophoresis as a new force field for field-flow fractionation",** Biophysical Journal, vol. 73, no. 2, 1997

44. Yager,P., **"Microfluidic diagnostic technologies for global public health"**, Nature, July 2006

45. **http://cels.uri.edu/news/archive/NewsNSF.html**

46. Dittrich, P. and Manz, A., **"Lab-on-a-chip: microfluidics in drug discovery"**, Nature Reviews Drug Discovery, March 2006

47. **http://www.physorg.com/news78508313.html**

48. Barden, S. et al. **"Volume-phase holographic gratings and their potential for astronomical applications"** Proceedings SPIE vol. 3355. Optical Astronomical Instrumentation, 1998

49. Barden, S. et al. "**Volume-Phase Holographic Gratings and the Efficiency of Three Simple Volume-Phase Holographic Gratings"** Publications of the Astronomical Society of the Pacific, volume 112 (2000), pages 809–820

50. **Change, D., Lorie, S. "Separation of bioparticles using the travelling wave dielectrophoresis with multiple frequencies",** IEEE Conference on Decision and Control, December, 2003.